APPLICATION OF HOLOGRAPHIC PARTICLE IMAGE VELOCIMETRY IN BUBBLY FLOW

By

ATANU BANERJEE

Bachelor of Technology in Mechanical Engineering

West Bengal University of Technology

Kolkata, W.B., India

2010

Submitted to the Faculty of the
Graduate College of the
Oklahoma State University
in partial fulfillment of
the requirements for
the Degree of
MASTER OF SCIENCE
May, 2013

APPLICATION OF HOLOGRAPHIC PARTICLE

IMAGE VELOCIMETRY IN BUBBLY FLOW

Thesis Approved:

Dr. Khaled Sallam

Thesis Adviser

Dr. Frank Chambers

Dr. David Lilley

Name: ATANU BANERJEE

Date of Degree: MAY, 2013

Title of Study: APPLICATION OF HOLOGRAPHIC PARTICLE IMAGE VELOCIMETRY IN BUBBLY FLOW

Major Field: MECHANICAL AND AEROSPACE ENGINEERING

Abstract: Measuring the velocity field of a bubbly flow is of major importance in many industrial applications like, bubble column reactors. Traditional PIV setup is limited to single plane measurements. The present study involved extension of the existing holographic PIV method to two-phase flow velocimetry. The objective of the present study was to conduct velocity measurements using in-line holographic microscopy arrangement to analyze a flow consisting of an air bubble rising through stagnant water in a rectangular column. Neutrally buoyant 8 μm sized hollow glass spheres are scattered uniformly in the continuous phase and are used as seed particles for image analysis. . Double-pulsed hologram is taken with a 2K by 2K pixels CCD sensor with 200μs in between the two frames, which allows only a small movement of both the particles (in the continuous phase) and that of the dispersed phase itself. Holograms are reconstructed at different distances to produce images at every millimeter of the measurement volume. An averaging technique is developed to process the images to reduce the noise in reconstructed holographic images and make it useful for cross-correlation analysis. The image pairs are cross correlated and velocity vectors are obtained for the continuous phase. The dispersed phase velocity is measured using the shift in the center of the bubble. After analyses of all the image pairs throughout the measurement volume, a two component three dimensional velocity field is produced for the two-phase flow.

TABLE OF CONTENTS

Chapter Page

LIST OF TABLES

Table Page

LIST OF FIGURES

Figure Page

Figure Page

CHAPTER I

INTRODUCTION

1.1 Background

Multiphase flow has wide industrial application. Many industrial processes rely on multi-phase phenomena for transport of energy and mass or for material processing. Multiphase flow can be of many types like gas-liquid, solid-liquid, solid-gas or particle laden gas-liquid flows. Out of this gas-liquid flow, dispersed gas bubbles in continuous liquid phase or liquid droplets in gas phase, is very common and found in many applications like liquid atomization, bubble column reactors, cavitation in turbo machineries, etc.

Velocity field measurement in single phase flow is done by many established techniques, but applying them in multiphase flow has its own challenges. Accurate velocity field measurements of both the phases will lead to better models for industrial operations and better understanding of the physics of the interaction between the phases. However more sophisticated measurement technique has led to the improved process control and quantification of fundamental parameters (Crowe, 2005).

This literature review describes various studies done in velocity field measurement of multiphase flow, its challenges and ways of solving it. The studies are described under three major topics PIV, ILIDS and Holography.

1.2 Challenges in Multiphase Velocimetry

Multiphase Velocimetry is sometimes stated as the final frontier of the flow velocimetry. Several things needed to be accounted for, to get the accurate velocity field.

1.2.1 Interaction between the liquid tracer particles and the gaseous phase

The interaction between tracer particles, also known as the seed particles, present in liquid with the dispersed gaseous phase can be a significant source of error, e.g., the tracer particles can have phobicity to the dispersed phase which may lead to low concentration of the tracers near the interface this in turn will lead to erroneous measurement near the bubble surfaces. If the tracers have affinity for the dispersed phase they will settle on the bubble-liquid interface making it more rigid and make it behave like a particle. This rigidness decreases the internal circulation and decreases the bubble velocity (Hassan et al, 1998). A significant drop in bubble velocity was measured mainly for bubble diameter smaller than 3mm (Lindken and Merzkirch, 2000). Later investigation on the particle size dependence of this interaction was studied and it was found that tracer particles having diameter smaller than 8μm have a significant influence but particles larger than 8μm diameter or having porous surfaces do not significantly interact with the dispersed phase (Yamamoto et al, 2001). Difference in bubble shape with and without the tracer particles have been noticed (Hassan et al, 1998) which can be explained on the basis of interaction of the tracer particles with the bubbles, although clear reasons for it is not yet known.

1.2.2. Phase separation

If a two-phase flow, like bubbly flow with low concentration of the dispersed phase is measured using a conventional setup, it will yield velocity field but identification of the velocity vectors with its phase or analysis of individual phase will not be possible. Hence phase separation is one of the most important criteria in multiphase velocimetry. Although only PIV is able to predict both phase data simultaneously but these techniques can be extended for other procedures like holography, LDA, etc. Also a flow can have a vast dynamic range, i.e., bubbles of different sizes which have different speeds, so assigning velocity vectors to different bubble sizes is also very important and needed for accurate measurement. This is accomplished by techniques like ILIDS, holography, etc. Phase separation can be achieved by various techniques like using fluorescent marker for liquid phase, computer algorithms based on intensity or size thresholding and velocity difference in each phases. Sizes of the bubbles are generally calculated by calculating the spatial resolution of the fringes in bubble image taken in defocused plane.

1.2.3. Density of the dispersed phase

Good measurements are achieved in case of low dispersed phase concentration but when concentration of dispersed phase is high it creates a huge problem, like, in dense bubble swarm the bubble images get overlapped or blocked by the bubbles in the front and it becomes difficult to analyze individual bubble, sometimes the density is so high that the light source doesn't crosses the whole measurement section or gets diverted in different directions, like, in liquid jets the area near nozzle region acts like a cylindrical lens and affects the illumination. These problems are addressed by matching the refractive indexes.

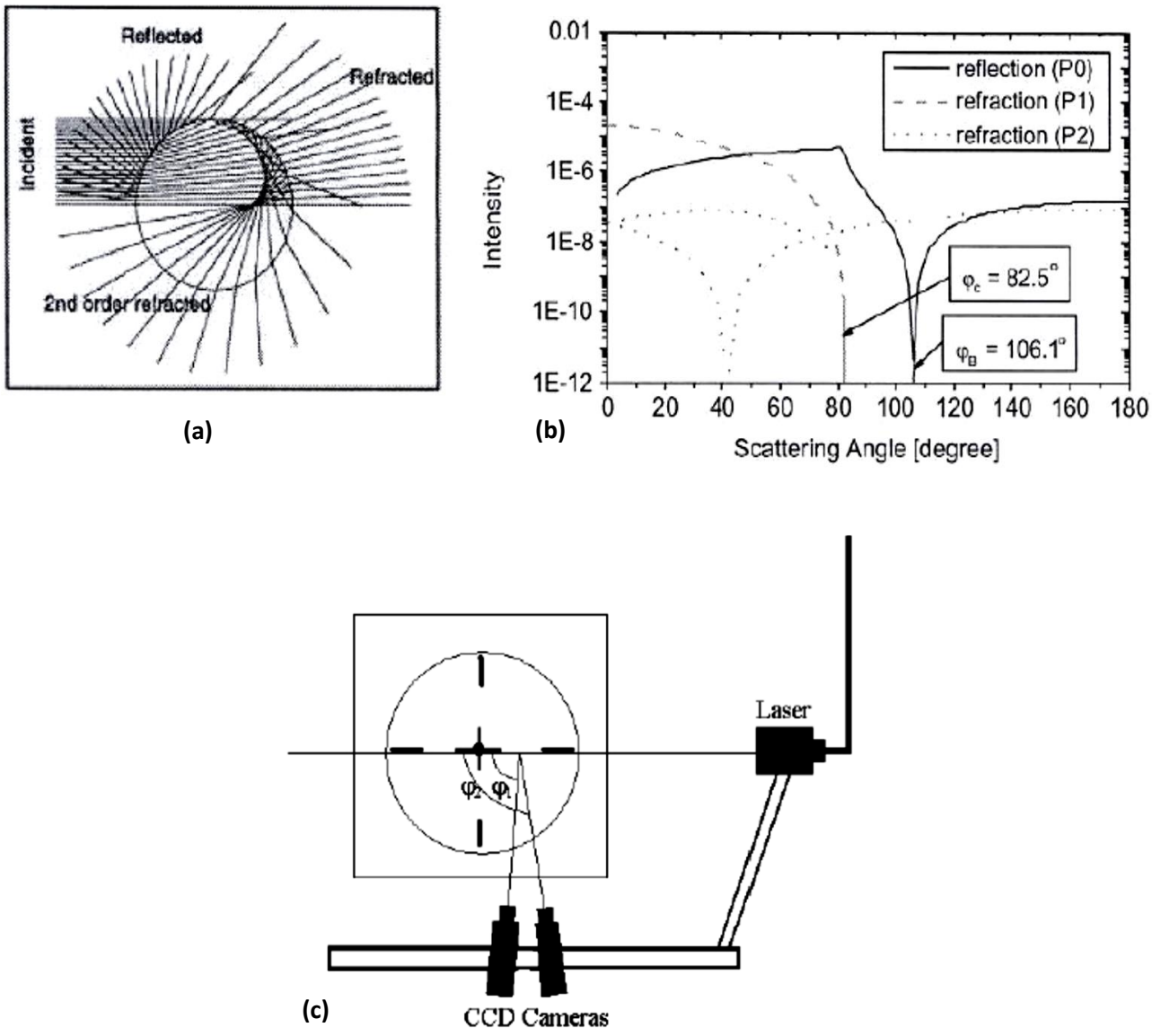

Fig. 1.1: (a) Air bubble in water, (b) Intensity of the different scattering modes as a function of the off-axis angle (M Honkanen, 2002). (c) Top view of the measurement setup, CCD recording image at different scattering angles (M Honkanen, 2002).

1.2.4. Different intensities of light scattered by bubbles and particles

Tracer particles and small bubbles both experience Mie scattering. The intensity (q) of the light scattered is dependent on the intensity of the incident light (I_0), wavelength of the light (λ), the polarization of light (γ), Diameter of the particle (d_p), the refractive index ratio (m) and scattering angle (φ) and is given by

$$q = I_0 \frac{\lambda^2}{8 \cdot \pi^2} i(\lambda, \gamma, \varphi, d_p, m) \tag{1.1}$$

Due to larger size of bubbles they have a higher intensity of light scattered than seed particles as shown in Fig. 1.1. This is good in separating the phases by intensity thresholding, but, if the bubble scatters a very high intensity of light a "blooming" effect occurs which overloads the CCD sensor elements showing white throughout the image. This is prevented by choosing a proper scattering angle to receive required intensity from bubbles.

1.2.5. Necessity of 3D measurements

2D velocimetry techniques are well established in single phase systems and have given reliable results for steady flows. Although having good resolution, 2D systems sometimes produce erroneous results for multiphase systems because the dispersed phase flow is highly 3D in nature and the dispersed phase cannot be tracked through successive image frames (Hassan & Canaan 1991), which leads to bad vector generation and if averaged may lead to quantitative inaccuracy. Multi-phase flows are often accompanied with turbulence which is a 3D phenomenon; hence without a 3D measurement system visualization will not be good from both qualitative and quantitative point of view. Some cases are shown in Fig. 1.2.

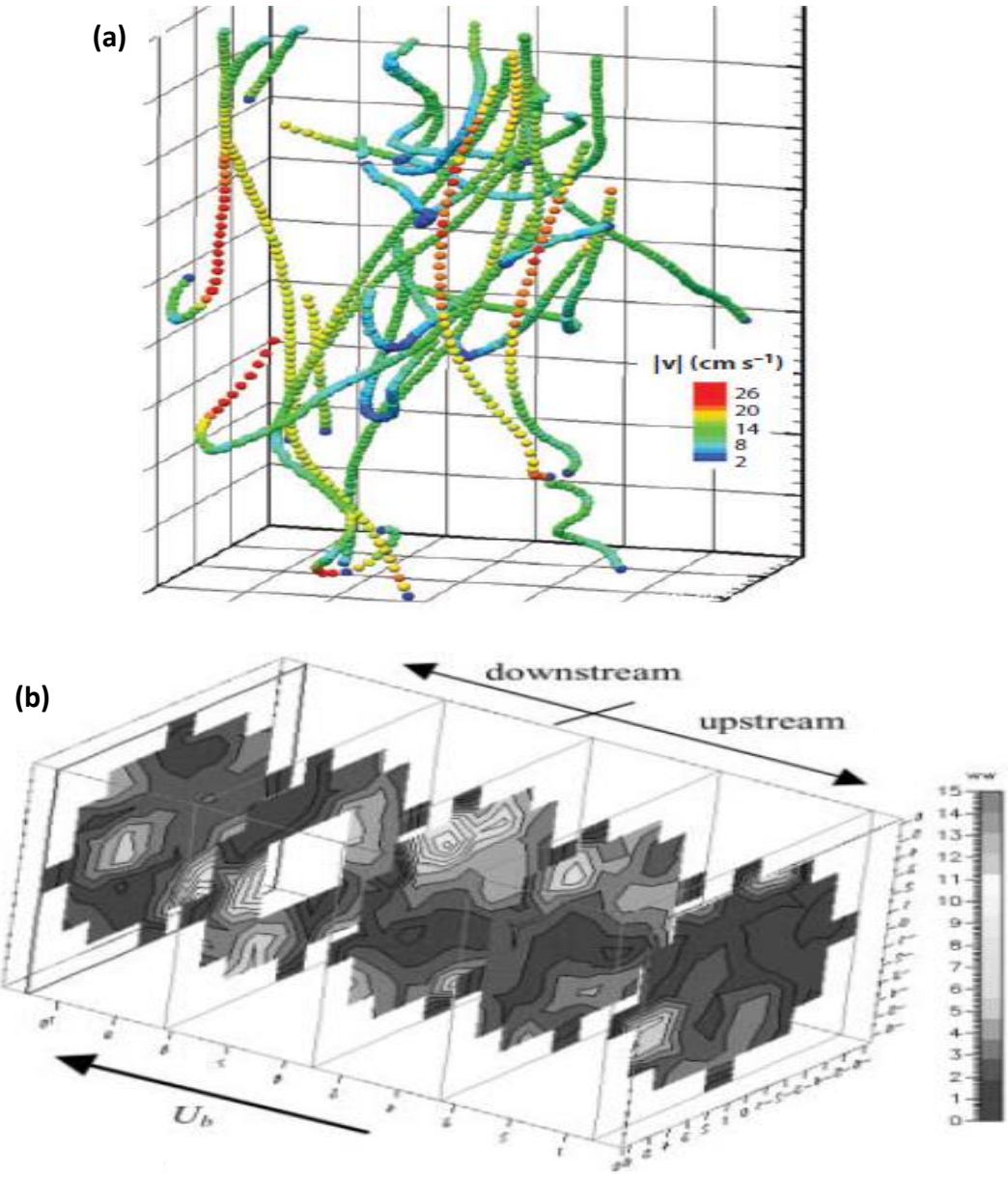

Fig. 1.2: (a) The 3D trajectories of the dispersed phase (Sridhar and Katz, 2001). (b) 3D velocity field of the continuous phase around the bubble (Ortiz et al, 2000).

General point of interest in multi-phase systems is dispersed phase size and velocity distribution, trajectory, wake structure of the continuous phase and its interaction with dispersed phase, etc. all of which are highly 3D phenomenon and can be well measured and understood only by 3D measurement systems. 3D systems gives us a larger amount of data than 2D systems so in cases where 2D systems are reliable, using 3D systems there will be more informative.

1.3 Previous works and their achievements

In this section previous experimental measurement of velocity vector field is discussed mainly for two phase flow. Three techniques have been used extensively to get flow field data, PIV, Holography and ILIDS. The works are categorized and discussed under individual techniques.

1.3.1 Holography

Holography, invented by Dennis Gabor in 1948, is a method by which phase and amplitude of a wave field can be recorded in a 2D plane. In normal photography only the intensity distribution is recorded and hence the information about the optical paths is lost (Hariharan, 2002). Whereas in holography a coherent illumination and reference beam from the same source is used to convert the phase information in variations of intensity and records it in a photographic plate. If the hologram is illuminated once again with same reference beam it reconstructs the original object wave. This is shown in Fig. 1.3. Image seen through the hologram perfectly resembles the 3D object with its original characteristics like depth of focus, etc.

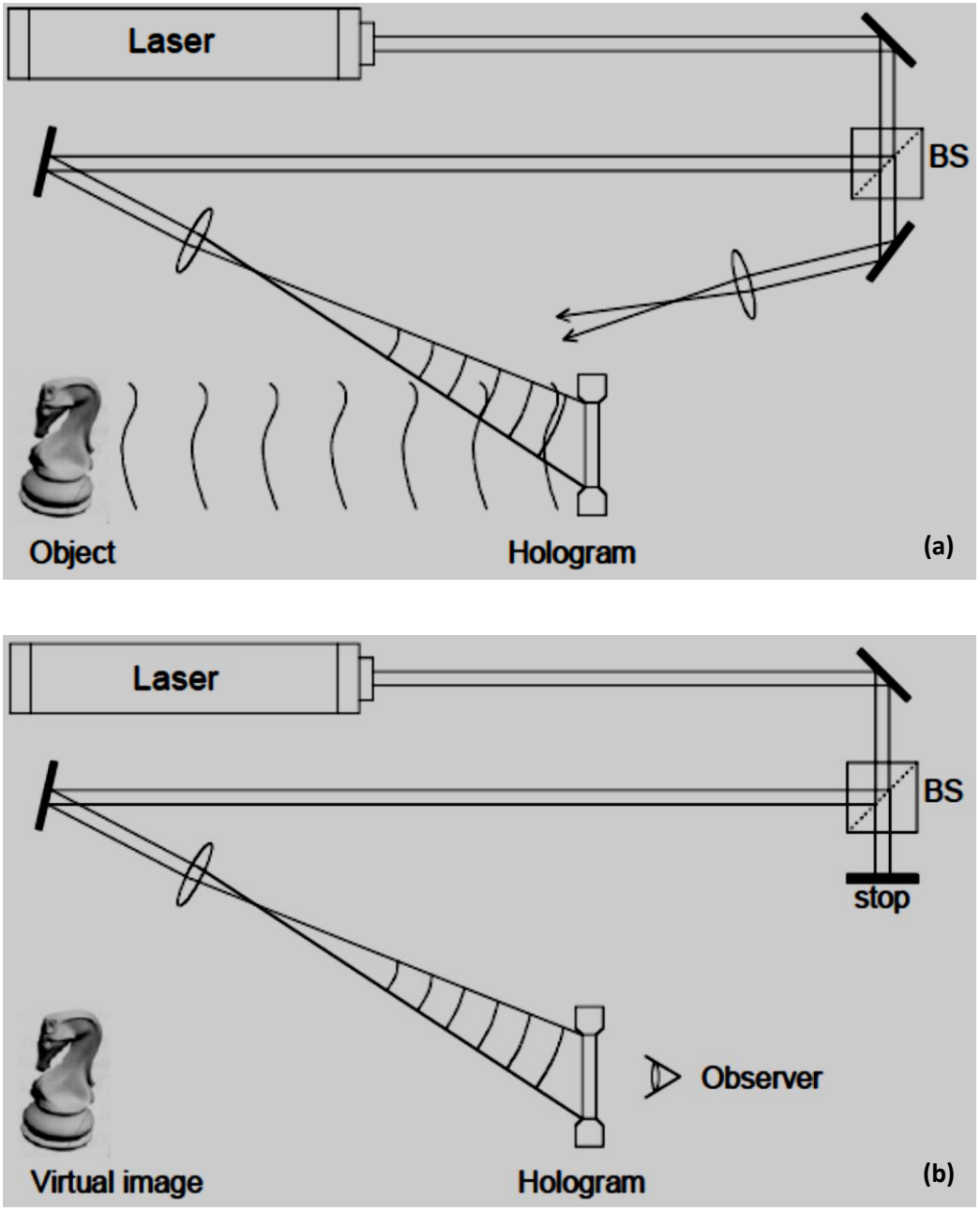

Fig. 1.3: (a) Hologram recording (Schnars and Jueptner, 2005). (b) Hologram reconstruction (Schnars and Jueptner, 2005).

1.3.1. (A) Digital Image Plane Holography

Burke et al (2002) introduced digital image plane holography, with application in spray diagnostics, where a defocused image is recorded by the camera and a collimated beam is used as a reference beam. This technique has the ability to measure size and position of the dispersed phase at multiplane (generally two planes). In this technique recording of both the planes is done simultaneously whereas reconstruction is done separately. Palero et al (2005) used this technique to measure the size and velocity field of air bubbles freely drifting in glycerin. A future of this technique can be measurement in two planes at 90^0 angles which will lead to 3D measurement of the dispersed velocity field.

1.3.1. (B) Hologram analysis technique:

With the recording setup of Palero et al (2005) the multiplexed hologram behaves as lenless Fourier hologram. The bubble diameter is calculated from the defocused plane by calculation of spatial fringe frequency like that of ILIDS technique. The main advantage of DIPH is that the overlapped particles in the defocused plane can be separated out in focused plane and back propagated to the defocused plane for measurement of bubble diameter as shown in Fig. 1.4 and Fig. 1.5. This technique is more efficient than optical compression technique by Maeda et al (2000) as evidence of horizontal overlapping in very dense dispersed phase condition is found.

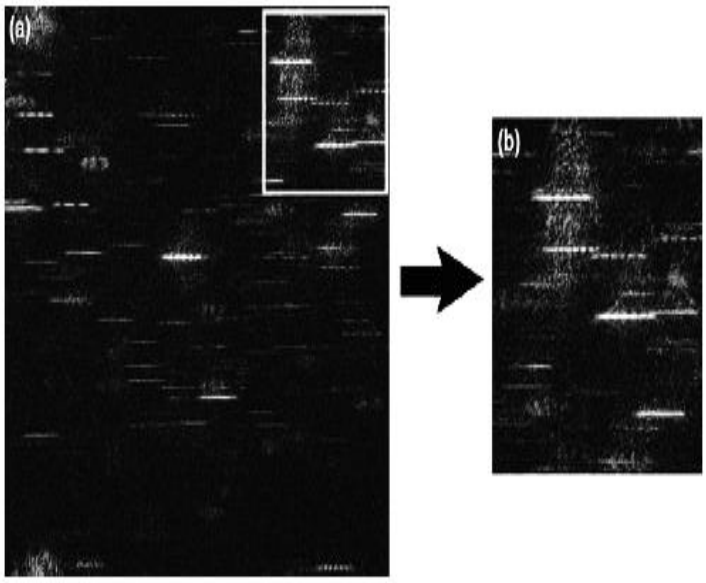

Fig. 1.4: Optical compression image (a) and the marked area are magnified in (b) which shows overlapping (Palero et al, 2005).

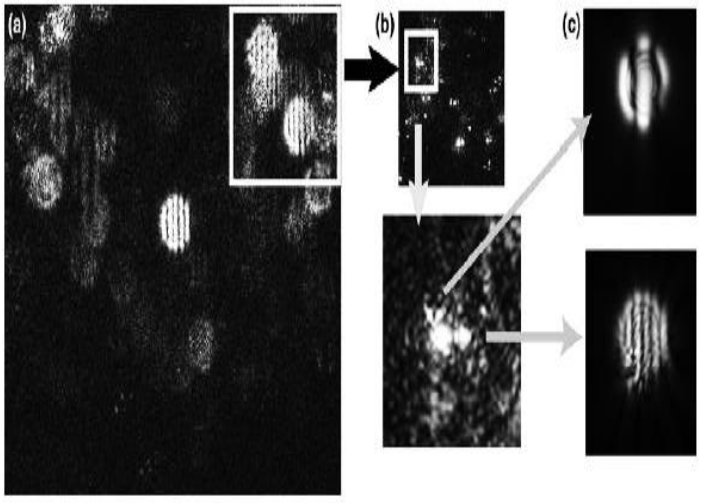

Fig. 1.5: The marked area in (a) is propagated in the focus plane (b) and two bubbles very close to each other can be visualized (Palero et al, 2005).

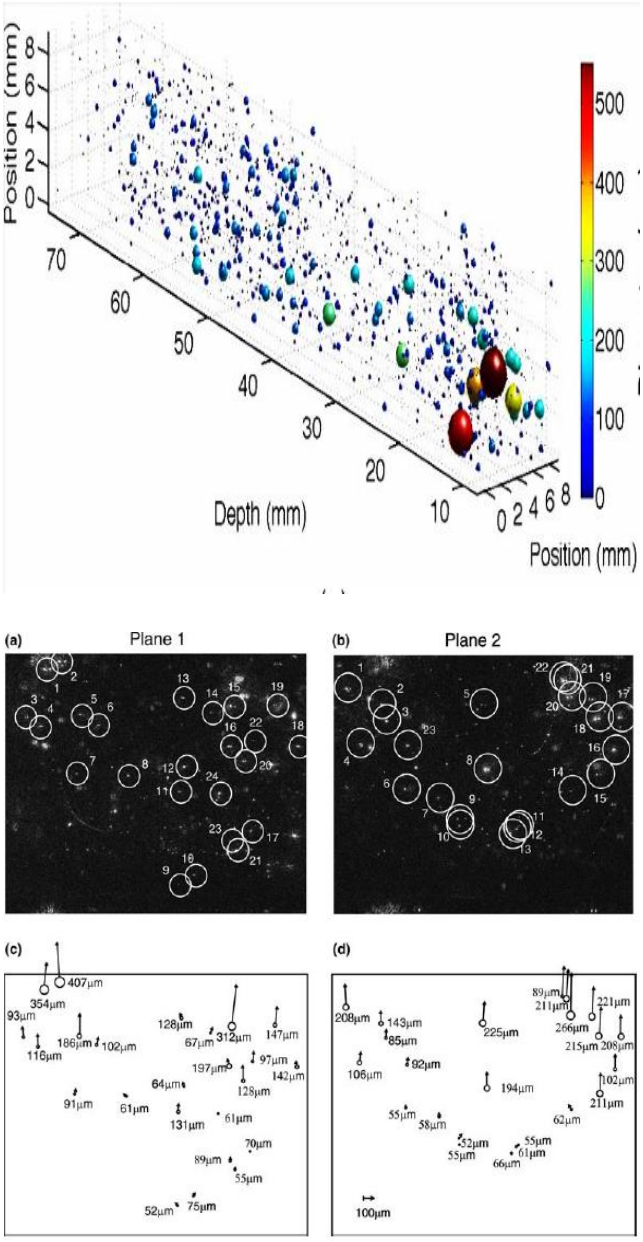

Fig. 1.6: 3D distribution of position and size of bubbles (Palero et al, 2005) (Tian et al, 2010).

1.3.1 (C) Location and velocity field for bubbles of different size

In a multi-phase system there can be bubbles of different sizes and velocity field for each of them should be available after measurement, so the dynamic range of the system is very important. Palero et al (2005) acquired the bubble images by a CCD camera (f=120mm, 1280X1024, 6.7μm/pixel). The visualized area is 12.1X9.7mm² in plane1 and 11.1X8.9mm² in plane2 with magnifications of 0.71 and 0.77 respectively. The minimum and maximum bubble diameter that can be measured by the setup is 36.9-600μm for plane1 and 35.1-717μm for plane2, which is wider than achieved by ILIDS technique. Also the technique allows higher particle density recording. Naito et al (2009) reports velocity measurement in 3D of milli and micro bubbles simultaneously, where milli bubbles are measured by stereo-shadowgraphy and micro bubbles (50-80μm) are measured by stereo-holography.

Tian et al (2010) reports 3D measurement of position and size of air bubbles in water ranging from 9-600μm using 1024X1024 pixel hologram in in-line setup as shown in Fig. 1.6, but no velocity data is found using that technique. But as measuring proper location of bubbles is very important for velocity so this technique can be extended to 3D measurement of bubble velocity.

1.3.1 (D) 3D velocimetry

Sheng et al (2006) measures 3D distributions, motions and trajectories of particles with an in-line setup. Naito et al (2009) reports 3D velocity measurements for micro and milli bubble using a single camera, in line holography as in Fig. 1.7. Measurement was done on a channel (1000X30X22mm), having micro bubbles (Dia. 50-80μm) and ellipsoidal milli bubble of air moving in water. CW YAG laser (λ = 532 nm) and CW He-Ne laser (λ = 632.8 nm) were used as

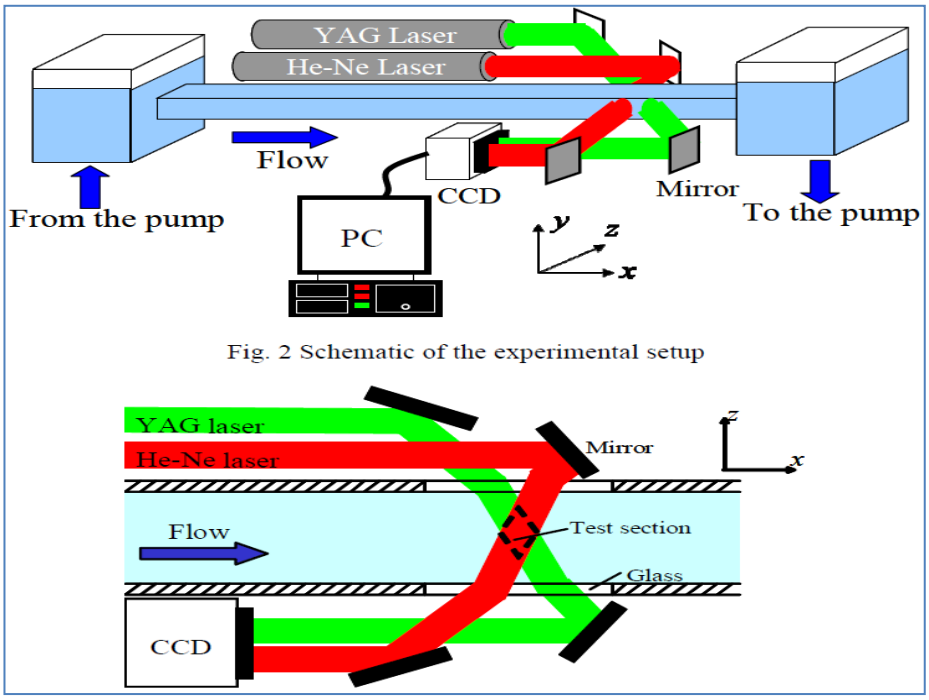

Fig. 2 Schematic of the experimental setup

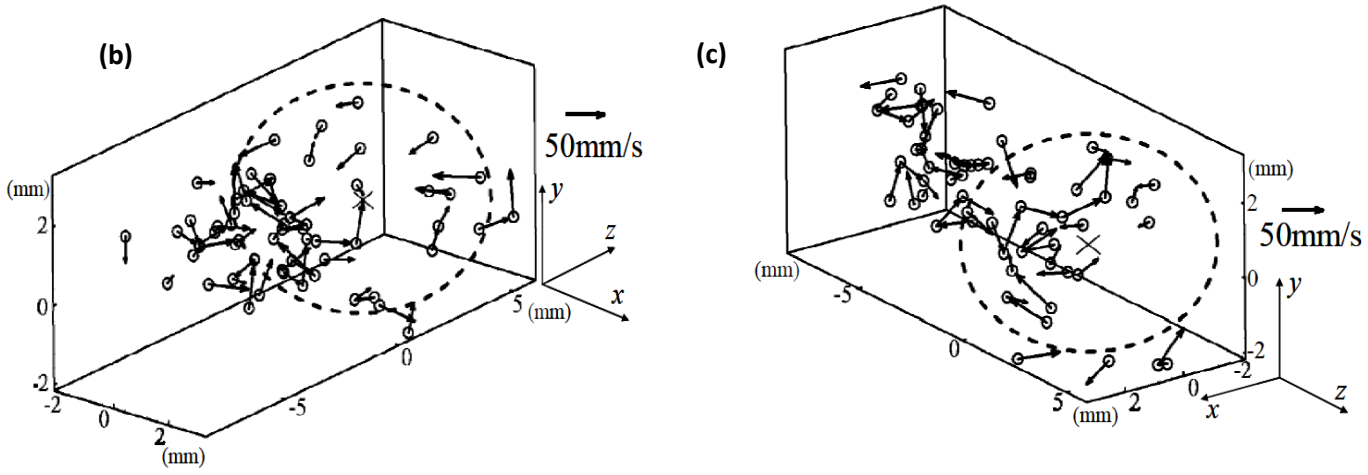

Fig. 1.7: (a) Experimental setup. (b), (c) Instantaneous position of milli bubbles and velocity vectors of micro bubbles; the result from different views based on same data (Naito et al, 2009).

light sources. Images were recorded by a 12 bit CCD camera (1920V1080, pixel size 7.4X7.4μm, 33 fps) with an exposure time of 50μs.

The technique of holography is inherently very efficient for 3D measurements and suitable for multiphase velocimetry compared to stereo schemes available in PIV, as it does not average between the two orthogonal views ,but, velocity measurements for both the phases is lacking in the literature. Until now the works using holography are done in either measurements of continuous phase or the dispersed phase only.

1.3.2 ILIDS (Interfereometric Laser Imaging for Droplet Sizing)

This technique came up as a transparent droplet/bubble size measuring technique from Koenig et al (1986). In conventional systems the droplets/bubbles are illuminated by a coherent light sheet. The reflection and refraction will create two glare points on the bubble surface as shown in the figure. When these droplets are seen by a camera at the focus plane the two glare points are visible but at the defocused plane they will superimpose to produce interference patterns as shown in Fig. 1.8. The spatial frequency of these interference patterns is proportional to the distance between two glare points and hence the droplet diameter.

$$d = \frac{2\lambda N}{\alpha}\left\{\cos\left(\frac{\theta}{2}\right) + \frac{n\sin\left(\frac{\theta}{2}\right)}{\sqrt{n^2 - 2n\cos\left(\frac{\theta}{2}\right) + 1}}\right\}^{-1} \quad (1.2)$$

This technique is later modified by Glovier et al (1995) for simultaneous measurement of several droplets and later Maeda et al (2000) used this technique for size and velocity measurement of spherical particles.

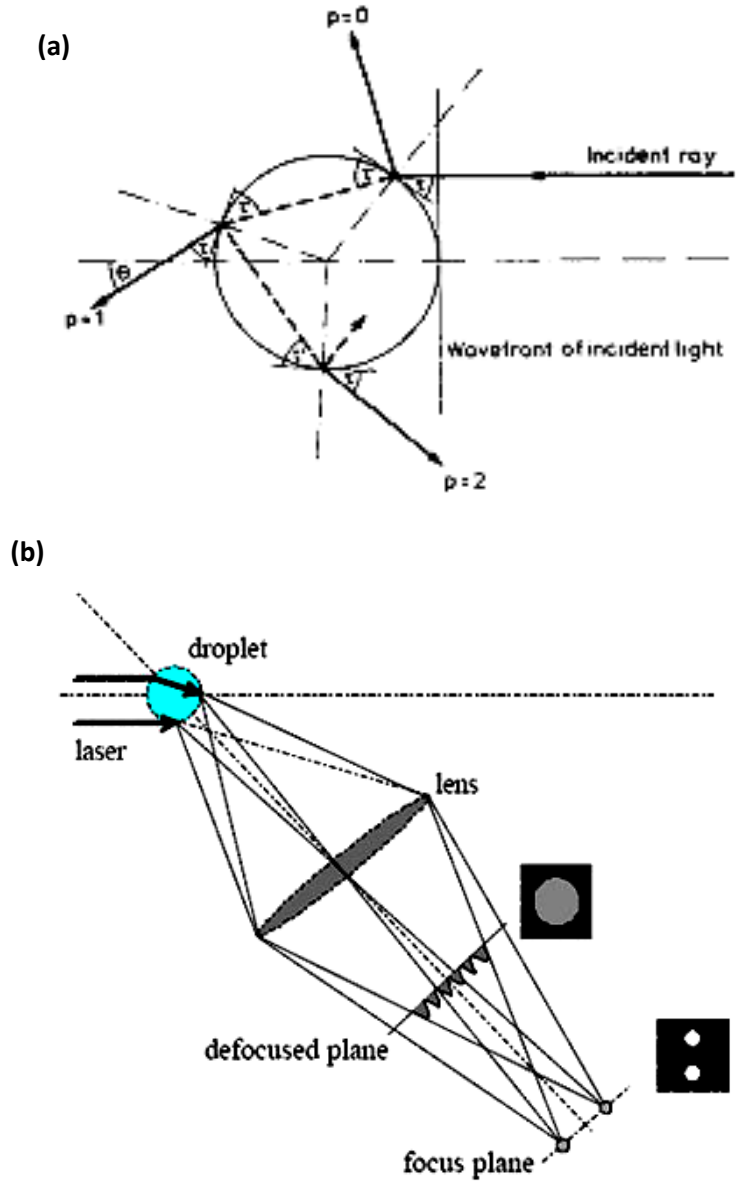

Fig. 1.8: (a) First order & second order refraction from transparent droplet. (b) Images taken at focused & defocused plane (www.velocimetry.net/application_ilids)

1.3.2 (A) Overlapping of bubble images

In measurement volumes having high density of dispersed phase the overlapping of the circular images is big problem in both size and velocity distribution measurement. This problem is addressed by Maeda et al (2000) by optical compression technique. Schematic of the optics is shown in the figure, a pair of cylindrical lens is used to generate the out-of-focus images on the focus plane and the rectangular aperture is to adjust the collecting angle and enhance the depth of the focus.

From the above image it is observed that with the optical compression technique 100 particles can be identified on the image whereas the conventional technique has difficulty to analyze 15 particles in the given area. The size of the circular image has no relation with the droplet/bubble diameter but it depends on the distance of the CCD camera from the particle. So these images cover a large area of the interferograms and moreover cause overlapping problems for dense dispersed media conditions.

1.3.2 (B) Particle size, location and velocity measurements

Maeda et al (2000) achieves the size and velocity of the particle as shown in Fig. 1.9. The discrete power spectrum provides a broad distribution and it becomes difficult to determine the real peak frequency. They adopted a fitting method for peak determination with sub-pixel accuracy in frequency domain. It was found that each signal has two components, the high frequency component tells about the particle diameter and the pedestal one tells about the location. The experimental setup has a camera of 1000X1000 pixels, with each pixel of 9μm^2. The measurement area is 10mm^2 with magnification 1:1 the scattering and

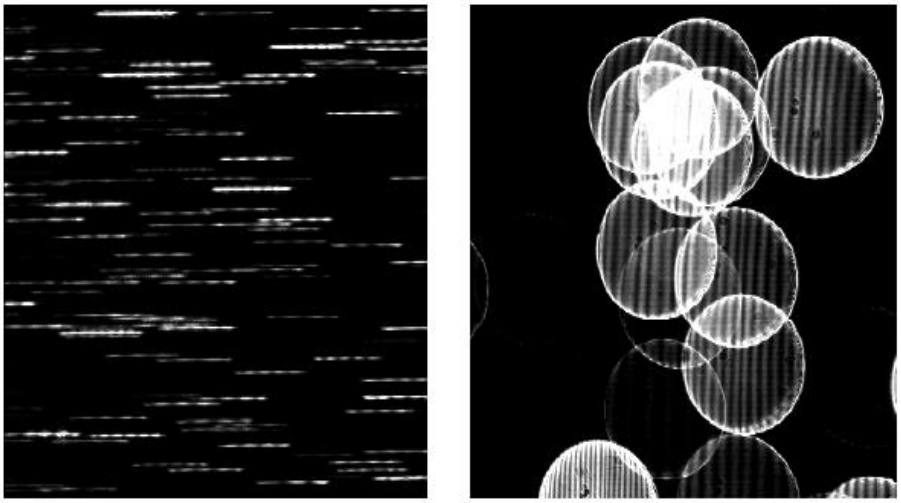

(a) (b)

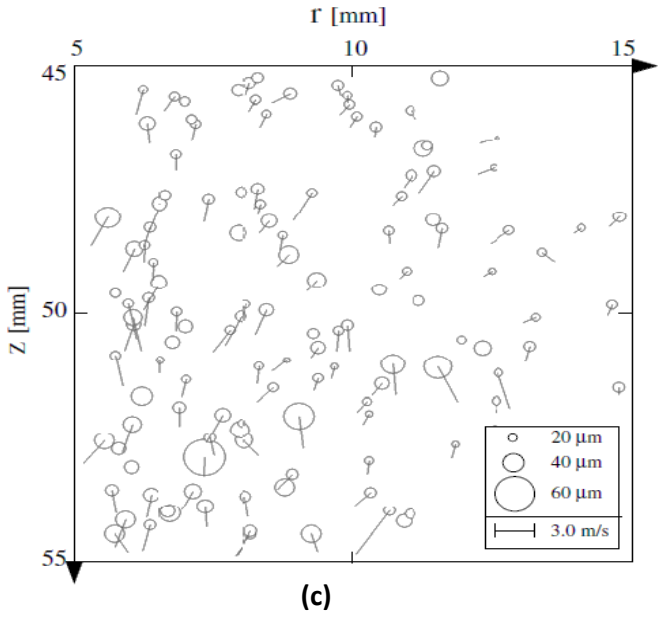

(c)

Fig. 1.9: An example of the portion measured of the interferometric image (4X4mm^2). (a) Using optical compression technique. (b) Conventional. (c) Instantaneous distribution of droplet sizes and velocity (Maeda et al, 2000).

collecting angle is set respectively at 70° and 12° respectively. The system analyzed is a DELAVEN nozzle with a flow rate of $5.3X10^{-}$ 7 m^3/s, for velocity measurements the maximum displacement between two images is 5X5 pixels and the laser pulse interval is 10-100μs. It was found that error of average diameter is less 3% and velocity measurements for particle concentration of 2.4 $X10^3$ /cm^3 is done. Lacagnina et al (2011) performed ILIDS measurement on cavitation bubbles downstream of propeller. The Nd:YAG laser (532 nm, thickness 2mm, output energy of 220mJ per pulse)illuminates a region of about 15X15cm^2. Camera resolution having 1280X1024 pixels, interval between two exposures is 120μs. The measurement section was located 1D downstream of the propeller having diameter 22.7 cm and turns clockwise at 20Hz. The system is able to measure bubbles of size 30-300μm and velocities upto 3 m/s is measured. Instantaneous bubble velocity is measured by cross-correlating each image pair of the acquired sequence. Averaging all the velocities in the data set at different positions an average velocity field is found but vectors generated in the tip vortex region is erased as it doesn't lie in the focus plane of the camera so measurements of that region are not accurate. The system has a limitation of bubble density of 50 per cm^3. This is demonstrated in Fig. 1.10.

1.3.2 (C) Limits of ILIDS

This technique is very effective in measuring droplet/bubble size and velocity simultaneously but is limited to transparent particles. Although various modifications in image processing technique is done but it is not applicable for very dense disperse medium concentration. The requirement for refractive index is not necessary for study of water sprays in air (Maeda et al 2000), which is a major problem in other techniques but measurement of air bubbles in water channels do require refractive index matching (Lacagnina et al 2011). Although the measured range of diameter size

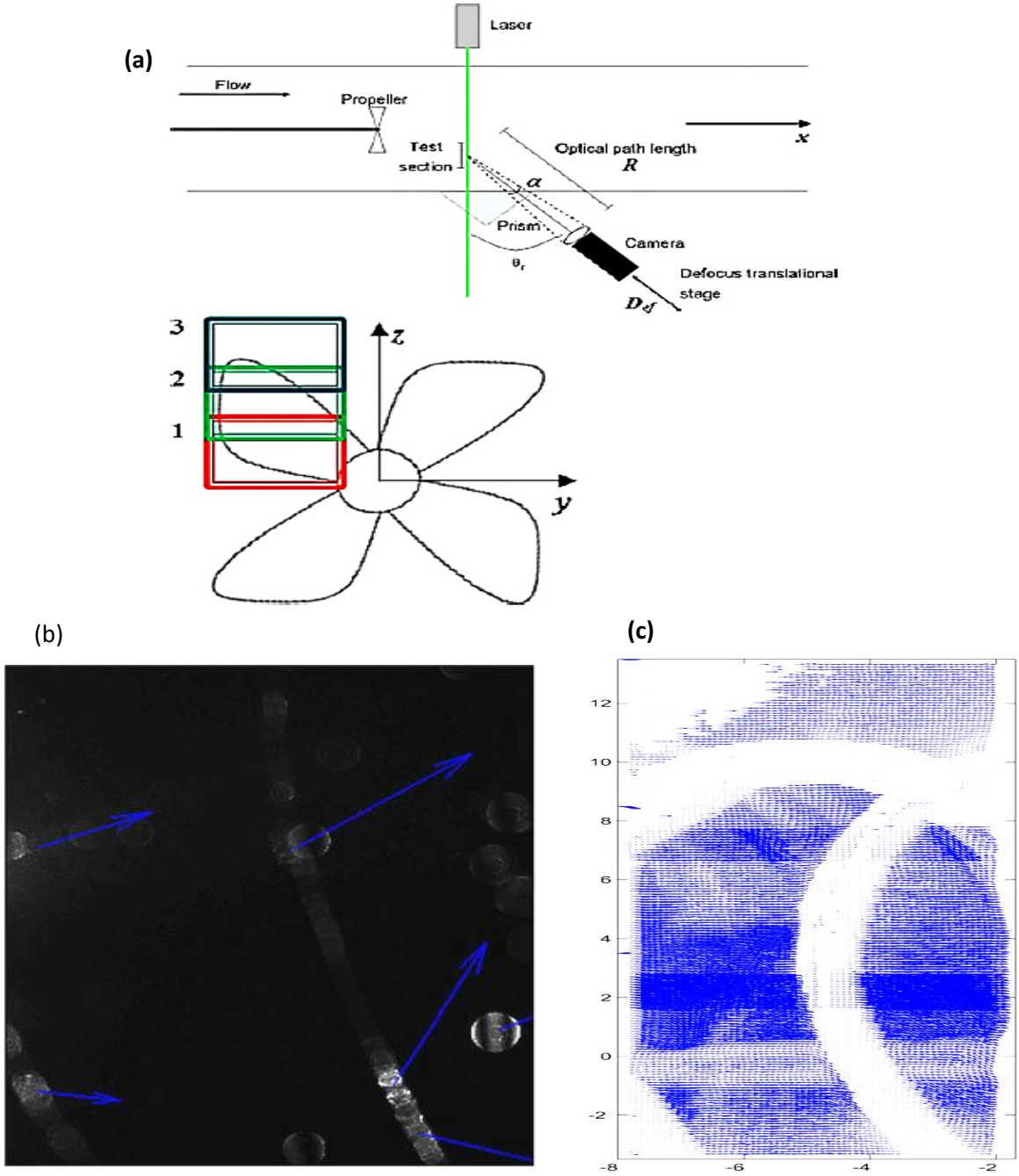

Fig. 1.10: (a) Experimental setup for three different measurement regions on the propeller model. (b) Instantaneous velocity vector field. (c) Mean velocity field after erasing vortex region (Lacagnina et al, 2011).

is good but there exists a limit of particle size measurement for a given experimental setup (Lacagnina et al 2011). Limit due to geometrical optics, i.e., to consider only reflected and first-order refracted rays rather than only Mie scattering is possible only when

$$\chi = \frac{\pi d_{\min}}{\lambda} \geq 20 \tag{1.3}$$

Limit due to number of fringes, i.e., minimum number of fringes must be two

$$d_{\min} = \frac{K}{\delta_{\max}} \tag{1.4}$$

$$= \frac{4m\lambda}{\alpha}\left[\cos\left(\frac{\vartheta_r}{2}\right) - \frac{m\sin\left(\frac{\vartheta_r}{2}\right)}{\sqrt{1+m^2-2m\cos\left(\frac{\vartheta_r}{2}\right)}}\right]^{-1} \tag{1.5}$$

1.3.3 PIV (Particle Image Velocimetry)

PIV is a very well established technique in single phase. Hassan and Canaan (1991) was the first attempt to apply PIV in multiphase scenario. Since then it has travelled a long way and is the only technique to predict both phase data simultaneously. As discussed earlier applying a conventional setup can produce velocity field for multiphase flow but it can't assign those vectors to its individual phases or unable to separately analyze the two phases.

1.3.3 (A) Phase Separation

The first attempt by Hassan and Canaan (1991) is not able to analyze the two phases simultaneously as they don't have a scheme for phase separation. Hassan et al (1992) presented the first scheme of separating the phases by intensity thresholding. Intensity thresholding utilizes the fact that a bubble, which is generally of bigger size, scatters a light of brighter intensity. The

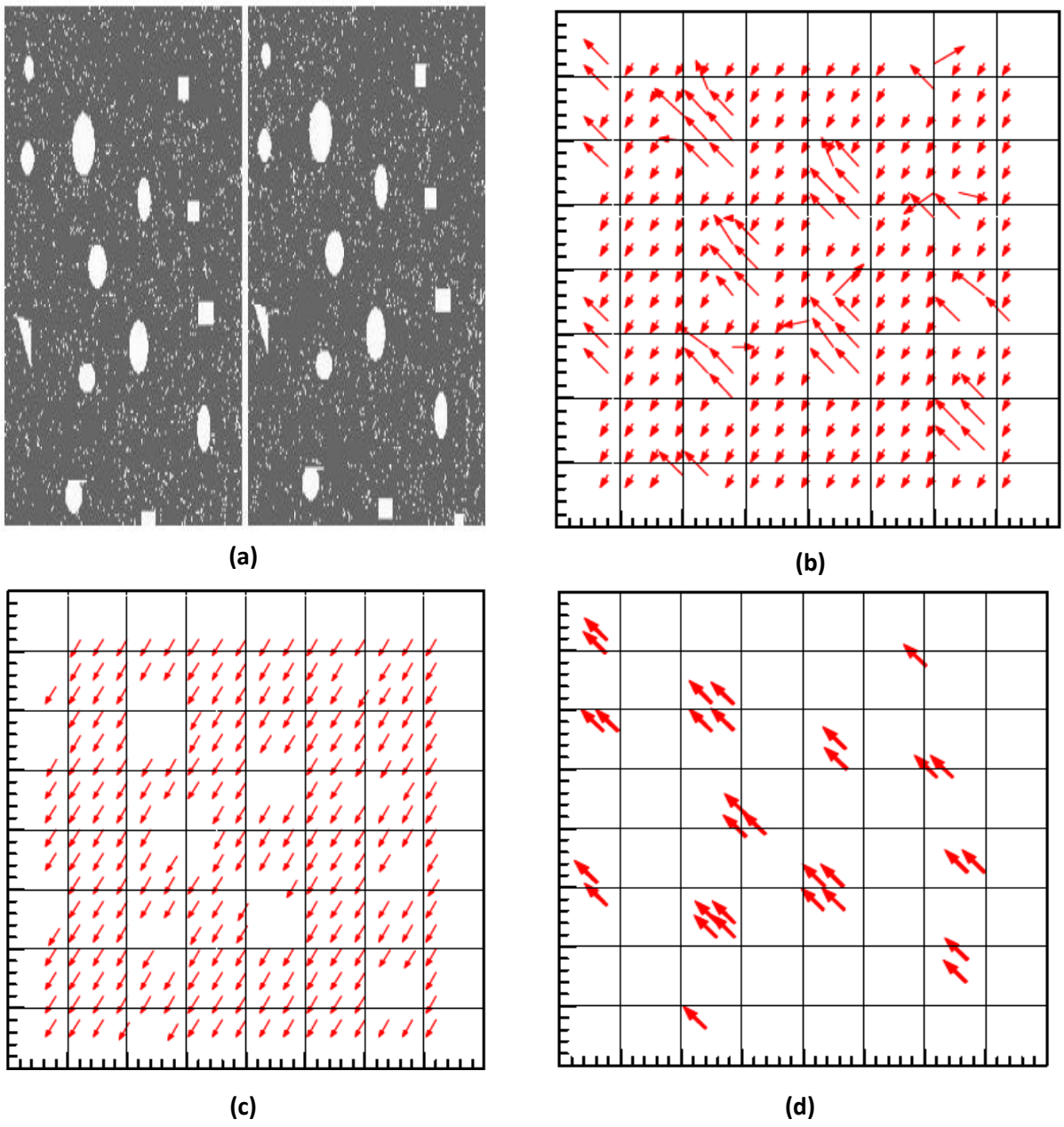

Fig. 1.11: (a)Simulated Image; (b) Results of cross-correlation technique; (c) Digital Mask technique for liquid phase; (d)Digital Mask technique for gas phase (Gui et al, 1997).

PIV image has both seed particle and bubbles in it, out of which bubbles are separated out by this technique.

Phase separation has also been achieved by introducing fluorescent markers in the flow (Sridhar and Katz 1995, Hassan et al 1993, Lindken and Merzkirch (2002) by which the tracer signals and Mie-scattered light from bubbles can be differentiated. Gui et al (1997) presented a digital mask technique which uses size thresholding together with Minimum Quadratic Difference (MQD). This technique is able to produce better results for comparatively high dispersed phase concentration with significant difference in velocity (both magnitude and direction) between the phases. The result of this technique on a simulated image is shown in Fig. 1.11.

From Fig. 1.11 it can be seen that the conventional cross-correlation technique generates bad vectors whereas the digital mask technique provides phase separated data with negligible number of bad vectors. Cheng et al (2010) developed a technique which is capable of simultaneously separating the two phases from stereoscopic PIV images as shown in Fig. 1.12. First the original PIV images are filtered by subtracting the background noise by using a FFT background filter that differentiates between seed particles and noise. Second, a relative intensity variation and a local maximum filter are applied. Finally the two phases can be easily distinguished and can be separated based on their size and intensity distribution. The filtering technique is tested in particle laden jet in cross flow.

1.3.3 (B) 3D measurements of Multiphase flow

Reese et al (2005) developed a PIV setup and implemented on gas-liquid and gas-liquid-solid system for 3D, full field, instantaneous velocity, acceleration and hold-up measurement for each

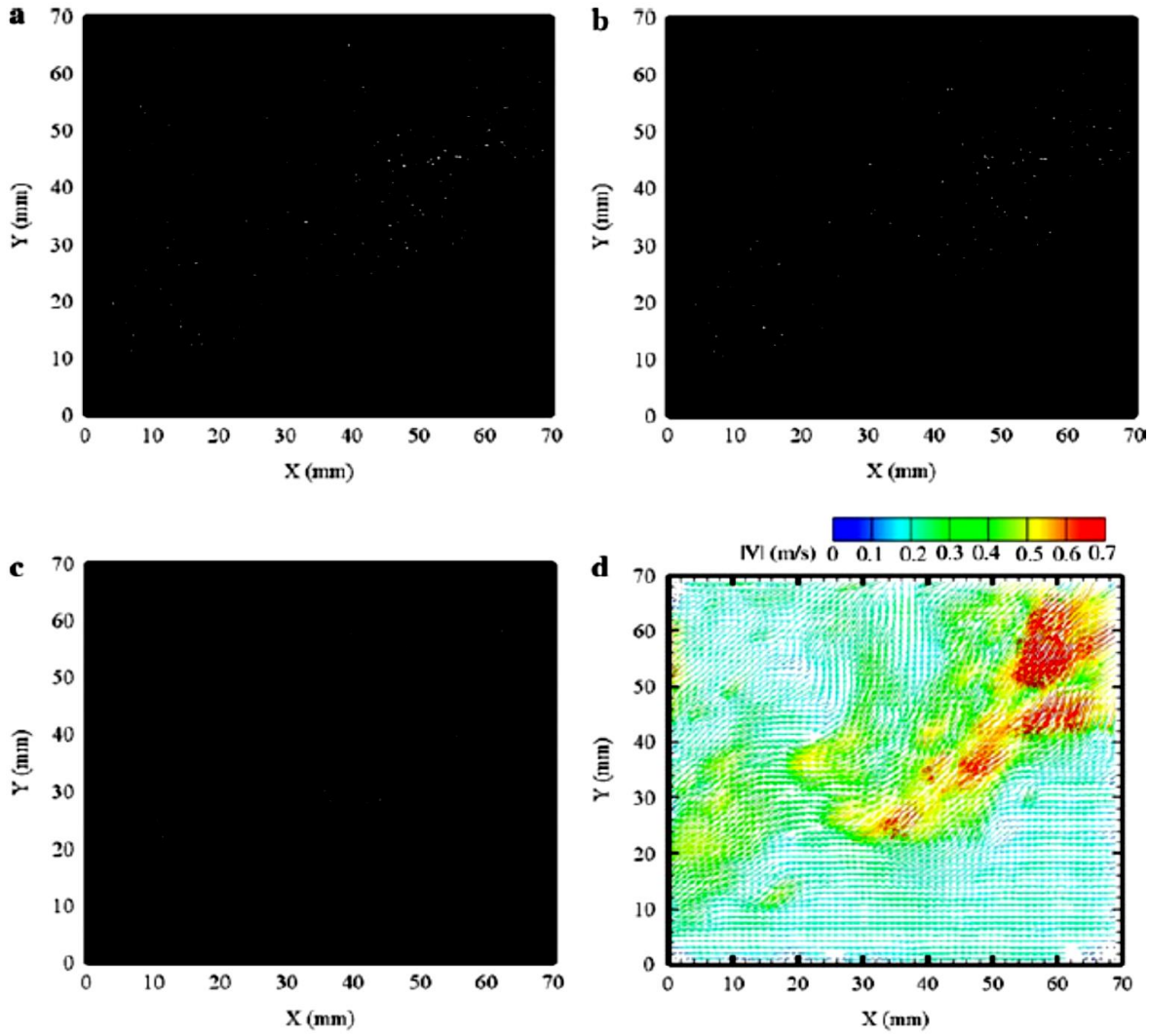

Fig. 1.12: The phase separation process demonstration of a particle-laden jet in cross flow with 70 mm X 70 mm field of view showing (a)the original image;(b)the separated large particle phase;(c)the separated tracer phase;(d)the velocity field from PIV of the tracer phase (Cheng et al, 2010).

phase. A measurement area of 10cm X 8 cm is viewed with a resolution of 512 X 480 pixels. Time separation between each photograph is 1/30 seconds. The important part of this setup is that it uses a single camera to generate the 3D field

Correlation of two views of flow field taken orthogonally is used to generate the3-D flow field. The figure shows how the two views for each phase are used to produce the 3D velocity vectors for each phase. The qualitative results match well with the previous experimental data while the quantitative results were not accurate. Hassan et al (1998) developed a stereoscopic 3-D PIV system for study of turbulent structures of bubbly flow. The data acquisition system consists of 4 cameras, run at field mode with increased frame rate of 60 fps and a reduced resolution of 620 X 240. Velocity field is extracted from the two set of stereoscopically arranged camera by using a neural network algorithm which provides a better yield than cross correlation technique. Brucker (1999) combined PIV and light scanning technique. A digital high speed camera of resolution 512 X 512 pixels is used to measure an area of 3 X 3 cm^2. The in-plane components were obtained from cross-correlation of successive images. A Scanning light sheet technique is used to illuminate the flow in vertical region of the tunnel. This multi planar extension to PIV eliminated the problem of bubbles moving out of the vertical light sheet. The total scanning width is 2.4 cm in five planes separated by 0.6cm. The results presented represents 2-D data set in the form of velocity vectors on a grid with 21 X 41 equidistant nodes over a cross section area of 3cm X 6cm as given in Fig. 1.13 (a). Simultaneously bubble motion in 3-D is recorded using a stereoscopic arrangement. Ortiz-Vilafuerte et al (2000) developed a setup to measure 3-D, transient velocity field generated by a single air bubble rising through water by the help of PTV technique. CCD cameras are operated in field mode with resolution 640 X 240 pixels and 60 fps.

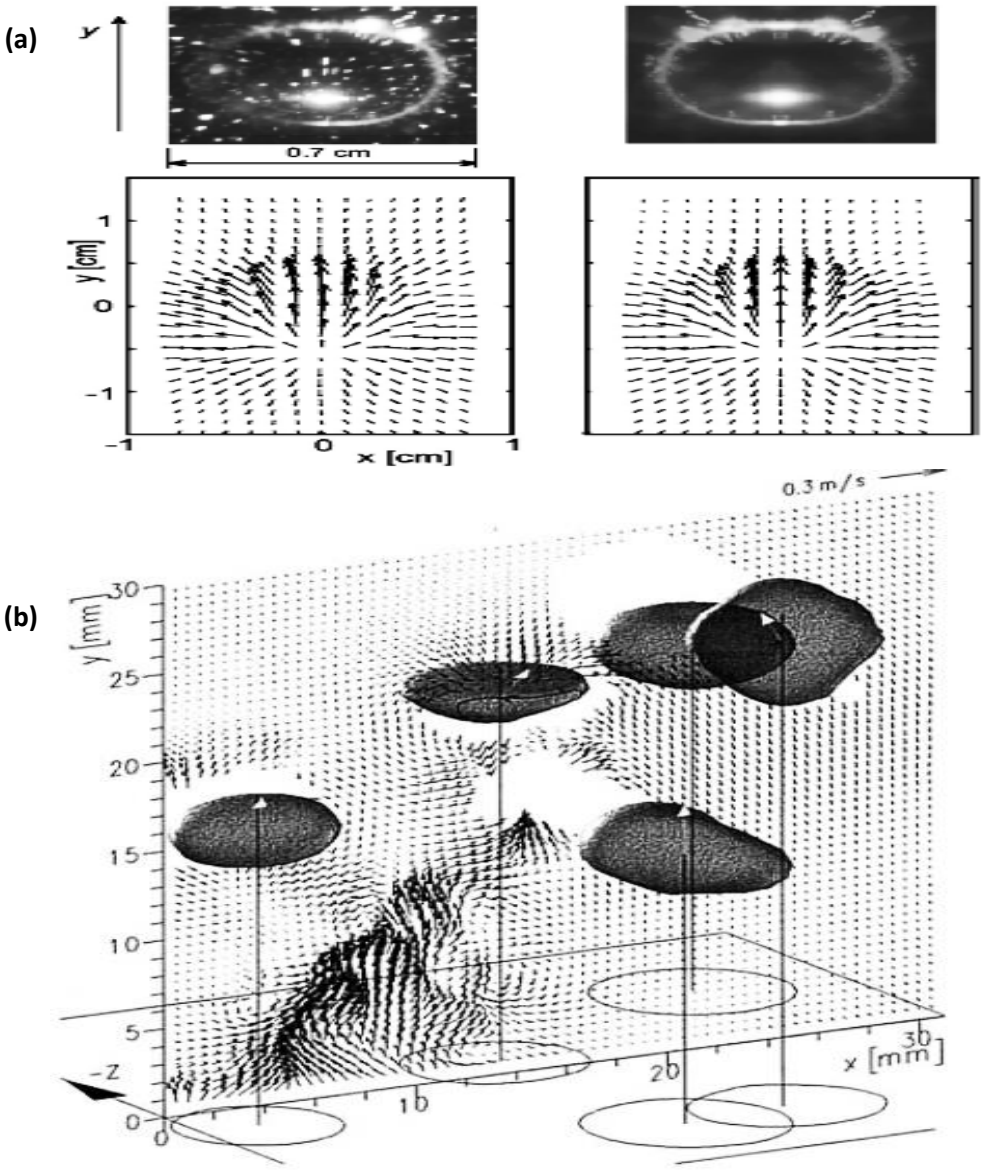

Fig. 1.13: (a) Bubble image and processed flow field in horizontal cross section (Brucker, 1999). (b) 2D velocity of the liquid phase and 3D velocity of the bubbles (Lindken and Merzkirch, 2002).

Although the system yields three dimensional information for turbulent quantities in a two phase system but higher spatial and temporal resolution needed to obtain accurate quantitative information. Lindken and Merzkirch (2000) analyzed a swarm of bubbles rising in water. The PIV setup was able to measure 2D-2C velocity of the liquid phase and 3D velocity of the bubbles as given in Fig. 1.13 (b).

Two CCD cameras, "Flowmaster 2" (1000 X 1000 pixels at 30Hz) and "Flowmaster 3" (1300 X 1000 pixels at 8Hz) are used in double shutter mode and 1.5 ms between two exposures. The 3-D position of the bubble is determined using a separate illumination and recording system using a high speed digital camera (512 X 512 pixels at 576 Hz). Digital mask technique is used to obtain phase separated data.

1.4 CONCLUSIONS

Holography seems to have produced best dynamic range in bubble velocity measurement and it is able to measure dispersed phase characteristics in most dense dispersed phase concentration with better resolution in at least two axes. Holography is well suited for three dimensional measurements compared to other techniques available, but, PIV is the only available technique which provides simultaneous measurement of both phases. So, the future path of work can be to make a holography setup which can produce 3D velocity field, with good spatial resolution for two phase flow.

.

CHAPTER II

METHODOLOGY

2.1 Introduction

This chapter elaborates on the methodology of the research, starting with description of the optical setup used for recording the hologram and details of the test section. Then the process of hologram recording and the numerical method of reconstructing the hologram are elaborated, with the cross correlation method for velocity analysis from reconstructed holograms. Finally validation of MATPIV results and stability of the system is analyzed along with the resolution of the optical setup.

Two shots of holograms are recorded using the CCD sensor with a very small time gap to ensure very small movements in the seed particles, to get the instantaneous velocity. Each of these holograms is then reconstructed every 1 mm of the measurement volume. The reconstructed image pair at a certain position is cross correlated to get a 2D velocity map for that position. This is repeated for each position of reconstruction and all these 2D velocity maps are stacked to get two component three dimensional (2C-3D) velocity map of the measurement volume. A schematic of the analyzing methodology is given below in Fig. 2.1.

2.2 Optical Setup

An in-line holographic microscopy setup is used with some modifications for achieving desired effects needed in this experimental setup. Two Nd:YAG lasers are used to achieve shorter time

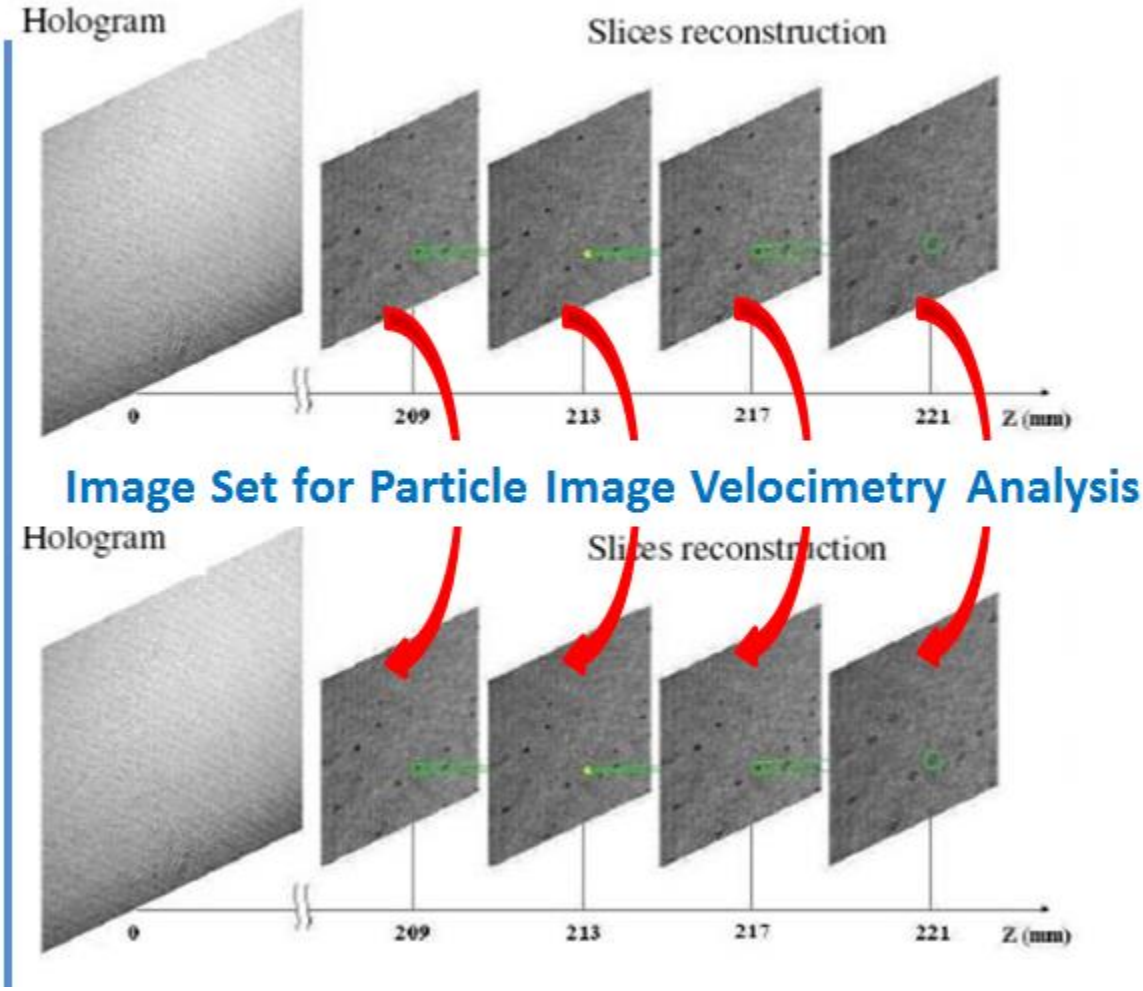

Fig. 2.1: A schematic of the analyzing methodology (modified from www.td.mw.tum.de/tum-td/de/forschung/themen/holomixers/NumReconstruction.jpg).

gap between two frames. Coherent light (λ=532nm) from the two laser sources is merged using a polarized beam combiner (PBC). It is passed through a polarizer and then projected on a polarized beam splitter (PBS). The PBS splits the beam in two parts, one of which is sent to an air-cooled beam dump and the other part is passed through a polarizer and then diverged by a microscopic objective after cleaning the beam through a spatial filter. The divergent beam is then passed through the test section to project it to the CCD sensor.

The polarizer before the PBS controls the amount of light going to the test section and the beam dump. The beam going towards the beam dump is kept as a substitute for use as a reference beam if needed. A separate reference beam is not used as the light passing through the test section acts as a reference beam itself and interferes with the diffracted beam from seed particles or bubbles. However this is valid until a certain concentration and at higher concentration values a separate reference beam is required. The CCD sensor electronically records the interference pattern, between the un-diffracted beam that passes through the test section and the diffracted beam from seed particles and bubble, which is the hologram in this experiment.

The test section consists of a plexi-glass container of dimensions 2.5 cm (W) X 8 cm (L) X 30 cm (H) with an air bubble injector with a nozzle diameter 0.279mm, fixed on the lower wall of the test section. Air is injected by an electric air pump. A schematic of the optical setup and the test section is shown below in Fig. 2.2. A list of all the components with specification and model number is given below in Table 1.

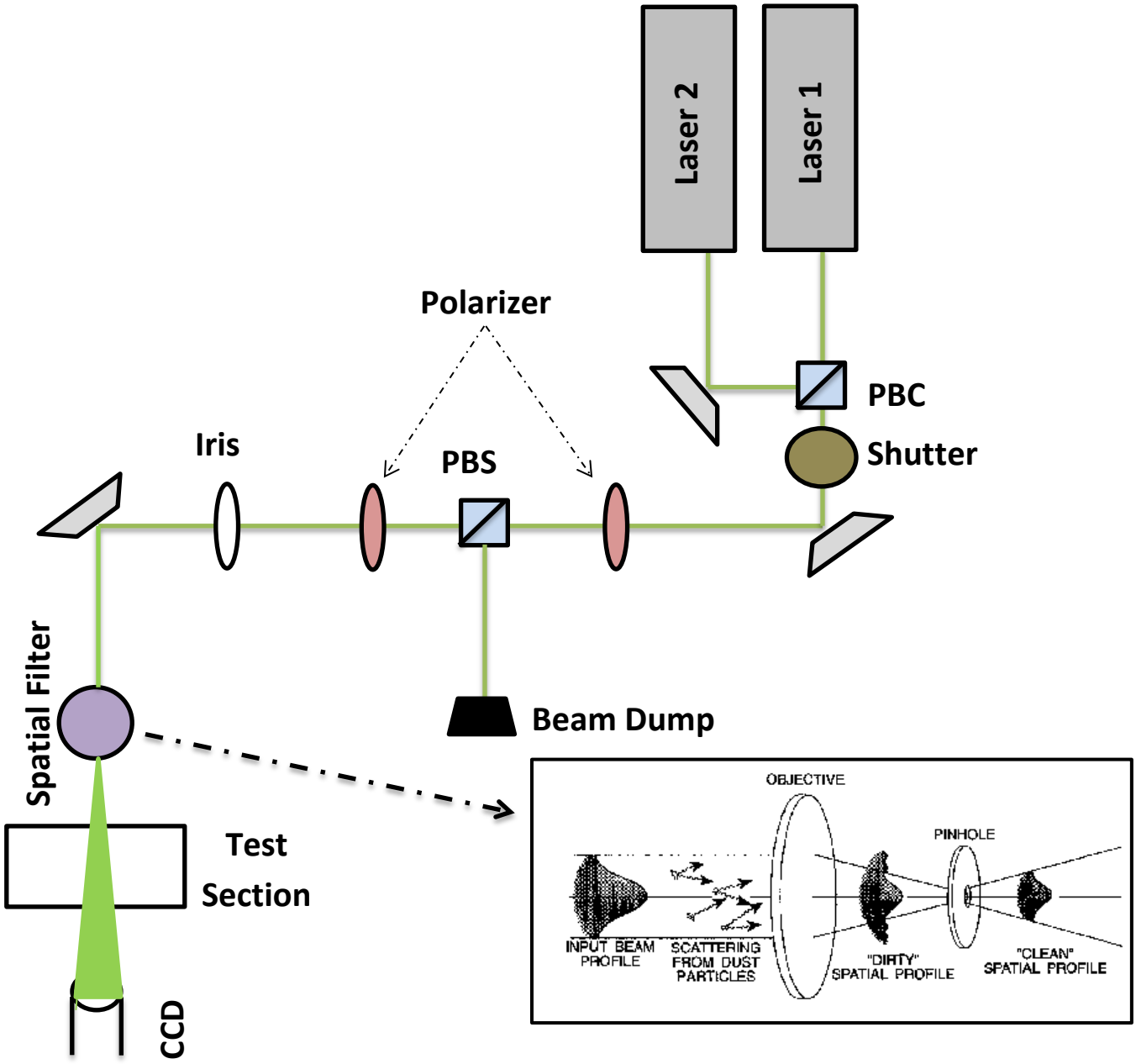

Fig. 2.2: A schematic of the experimental setup (Spatial Filter Schematic Ref.: www.jirkacech.com/public/Thesis/img230.gif).

Table 2.1: A list of components with model number and specifications.

Equipment	Company/ Model No.	Specifications
Laser	Spectra Physics/ Lab 150.	Nd:YAG, injection seeded, 200 mJ/p, 532 nm.
Photo Detector	Thor Labs/ Det210.	Silicon PIN, 200-1000 nm response, rise time 1 ns, 12V battery.
Laser Power/Energy Meter	Ophir/ Nova II.	Data transmission ~500pts/s, USB, RS232.
Camera	PCO/ 2000.	14bit CCD, 160 MB/s, 2048X2048 pixels.
Shutter	Uniblitz/ VS14S.	14mm aperture, 1.5 ms to open.
Seed Particles	TSI/ 10089.	Hollow Glass Spheres, MD 8-12µm, 1.05 g/cc, RI 1.5.
Pulse Generator	Quantum Composers/ 9518.	1ns timing resolution, 400 ps jitter, independent width & delay control.
Oscilloscope	Teledyne Le Croy/ 9314L.	300 MHz, 100MSa/s, 4 channels.
Anti-Vibrational Table	Newport/ RS 2000^{TM}.	M6-1.0 holes on 25 mm grid, Surface Flatness ±0.004

2.3 Recording Hologram

Digital holograms are recorded electronically on CCD (Charged Coupled Devices) sensors. CCD imaging is done in three steps.

2.3.1 Light exposure

The incident light is converted into an electronic charge at individual pixels or detectors, also known as 'internal photo effect'.

2.3.2 Charge transfer

The charge within the semiconductor is transferred to the memory cells.

2.3.3 Charge Conversion

Conversion of charge into voltage is done by the capacitor matrix and the output voltage is then amplified by an amplifier.

CCD cameras have different architecture and specifications. The specifications and a diagram of pco2000 camera used in this experiment are listed below in Fig. 2.3 and Table 2.2.

2.4 Reconstruction of Holograms

Digital holograms are reconstructed numerically using different approaches like Fresnel Approximation, Convolution Theorem, etc. It is the process of retrieving a 2D image from the 3D information stored in hologram. In this study both the holograms are reconstructed throughout the measurement volume at every 1mm distance using Convolution theorem which is discussed later. A schematic is shown in Fig. 2.4.

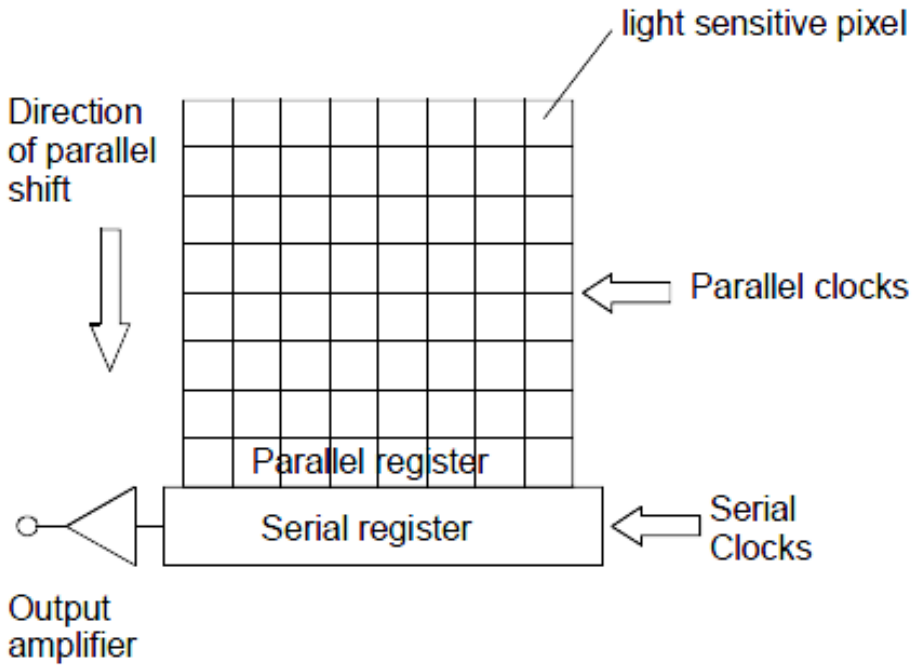

Fig. 2.3: Full-frame architecture CCD. (Ref.: Digital Holography, Schnars &Jueptner)

Table2.2: Specifications of the CCD sensor. (Ref.: 1288 sheet, pco2000)

Basic Parameters

	unit	setpoint	pco.2000
total quantum efficiency η_{mean}	%	@ 423nm	46.2
inverse of overall system gain 1/k (conversion factor)	e^-/DN^3	typical	2.1
saturation capacity $\mu_{e.sat}$	e^-		35 225
standard deviation of temporal dark noise σ_{d0}	e^-	@ 0s exposure time	9.0
dark current N_{d30}	e^-/s	@ 30°C housing temperature	tbd[4]
doubling temperature k_d	°C		tbd

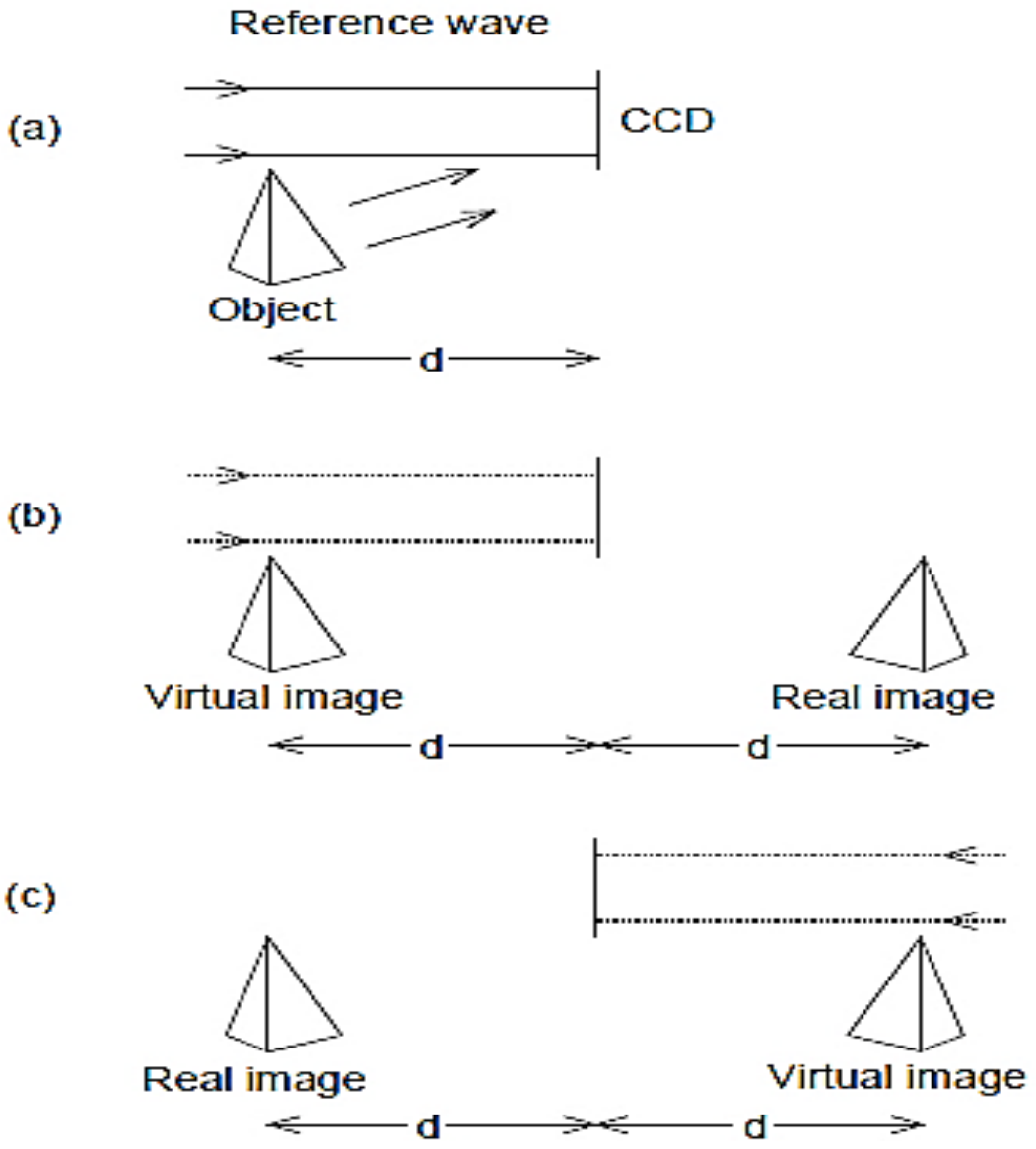

Fig. 2.4: (a) Hologram Recording.

(b) Reconstruction with reference wave E_R.

(c) Using reference wave E_R^*. (Ref.: Digital Holography, Schnars & Jueptner)

2.4.1 Numerical Methods

Digital holography has the possibility of looking at different object layers. In order to obtain high lateral resolution the CCD is placed near to the object. In such short distances Fresnel's approximation no longer works. The convolution approach is used.

The diffraction of a light wave at an aperture (in this case a hologram) which is mounted perpendicular to the incoming beam is given by the Fresnel-Kirchhoff's integral

$$\Gamma(\xi',\eta') = \frac{i}{\lambda}\int_{-\infty}^{\infty}\int_{-\infty}^{\infty} h(x,y)E_R(x,y)\frac{\exp\left(-i\frac{2\pi}{\lambda}\rho'\right)}{\rho'}dxdy \quad (2.1)$$

Where

$$\rho' = \sqrt{(x-\xi')^2 + (y-\eta')^2 + d^2} \quad (2.2)$$

where h(x, y) is the hologram function and ρ' is the distance between a point in the hologram plane and a point in the reconstruction plane. The angles θ and θ' are approximately zero and hence the inclination factor is set to one. The other geometrical quantities are illustrated through the Fig. 2.5.

Equation 2.1 is the basis of numerical reconstruction of hologram.

2.4.2 Convolution Approach

This was first used for reconstruction of sub optical holograms (Demetrakopoulus and Mittra 1974) and then latter in Optical holography (T Kreis 2002). To reconstruct an undistorted real image Er is replaced by Er* in the basic equation given by equation 2.1.

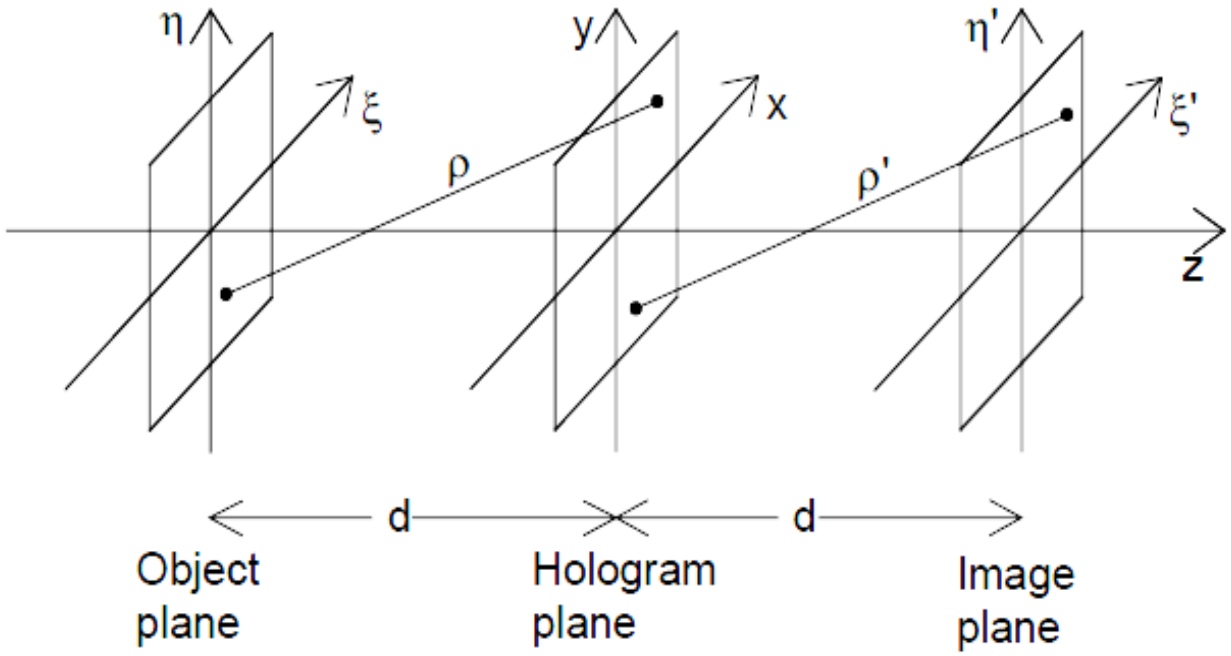

Fig. 2.5: Coordinate system for numerical hologram reconstruction. (Ref.: Digital Holography, Schnars & Jueptner)

The above reconstructed formula can be interpreted as superposition integral.

$$\Gamma(\xi,\eta)=\frac{i}{\lambda}\int_{-\infty}^{\infty}\int_{-\infty}^{\infty}h(x,y)E_R^*(x,y)\frac{\exp\left(-i\frac{2\pi}{\lambda}\rho\right)}{\rho}dxdy \tag{2.3}$$

With the impulse response g(x, y, ξ, η) given by

$$g(\xi,\eta,x,y)=\frac{i}{\lambda}\frac{\exp\left[-i\frac{2\pi}{\lambda}\sqrt{d^2+(x-\xi)^2+(y-\eta)^2}\right]}{\sqrt{d^2+(x-\xi)^2+(y-\eta)^2}} \tag{2.4}$$

As the linear system characterized by g (x, y, ξ, η) = g (ξ-x, η-y) is space invariant hence convolution theorem can be applied on the superposition integral. According to the convolution theorem the convolution of two functions is equal to the inverse Fourier transform of the product of each function's individual Fourier transforms. So Γ can be calculated by Fourier transforming h.Er* and then calculating its product with Fourier transform of g and finally taking an inverse Fourier transform of this product. The numerical impulse response is

$$g(k,l)=\frac{i}{\lambda}\frac{\exp\left[-i\frac{2\pi}{\lambda}\sqrt{d^2+\left(k-\frac{N}{2}\right)^2\Delta x^2+\left(l-\frac{N}{2}\right)^2\Delta y^2}\right]}{\sqrt{d^2+\left(k-\frac{N}{2}\right)^2\Delta x^2+\left(l-\frac{N}{2}\right)^2\Delta y^2}} \tag{2.5}$$

The reconstruction into the real image plane is

$$\Gamma(\xi,\eta)=\Im^{-1}\left\{\Im\left(h\cdot E_R^*\right)\cdot\Im(g)\right\} \tag{2.6}$$

The Fourier transform of g (k, y) can be calculated and expressed analytically by

$$G(n,m)=\exp\left\{-i\frac{2\pi d}{\lambda}\sqrt{1-\frac{\lambda^2\left(n+\frac{N^2\Delta x^2}{2d\lambda}\right)^2}{N^2\Delta x^2}-\frac{\lambda^2\left(m+\frac{N^2\Delta y^2}{2d\lambda}\right)^2}{N^2\Delta y^2}}\right\} \tag{2.7}$$

This saves one Fourier transform from reconstruction.

$$\Gamma(\xi,\eta) = \Im^{-1}\left\{\Im\left(h \cdot E_R^{*}\right) \cdot G\right\} \tag{2.8}$$

Numerical reconstruction using Fresnel-Kirchhoff's integral is time consuming. The convolution method operates faster and is very suitable for particle field measurements.

2.5 Velocity Analysis

The velocity vectors are calculated by cross correlating two images which are reconstructed at same distance from the CCD sensor. Holograms from which the images are reconstructed are recorded using a small time delay of 200μs between the laser pulses to find the instantaneous velocity. The cross correlation technique gives the 2D velocity map at a plane in the measurement volume. This is done throughout the measurement volume and stacked to find a two component three dimensional (2C-3D) velocity map for the test section.

2.5.1 Cross Correlation

The basic principle behind cross correlation is matching the pattern of particles found in one image with that of other. It involves dividing each image into smaller interrogation windows and cross correlating them with the corresponding windows of the other image at the same position taken at a different time instant.

Sveen and Cowen (2004) uses equations 2.9 and 2.10 below for calculating the displacement of the particles between the image pairs

$$R_e(s,t) = \sum_{m=0}^{M-1} \cdot \sum_{n=0}^{N-1} [\, I_1^{i,j}(m,n) - I_2^{i,j}(m-s,n-t)]^{2} \tag{2.9}$$

Equation 2.9 can be simplified as given below

$$R_s(s,t) = \sum_{m=0}^{M-1}.\sum_{n=0}^{N-1}[\, I_1^{i,j}(s,t).I_2^{i,j}(m-s,n-t) \qquad (2.10)$$

Here $I_1^{i,j}$ denotes the interrogation window in the first image with i, j as the row and column numbers. Similarly $I_2^{i,j}$ is for interrogation window in the second image. Equation 2.10 represents cross correlation for the terms in the interrogation windows of the two images which is the basis for the algorithm used in MATPIV, an open source MATLAB toolbox, to calculate velocity vectors from the reconstructed images.

2.6 Validation of Matpiv

The cross correlation analysis to get velocity vectors is done by MATPIV 1.6.1, developed by J K Sveen in 2004. This is an open source toolbox which is based on MATLAB platform. The results of MATPIV are validated with test images of known cases.

2.6.1 Test Image-An axisymmetric jet with PIV setup

A test image pair of axisymmetric jet is taken for PIV analysis. The images are given below in and these are processed with interrogation window of size 128 X 128 pixels. The resulting velocity vector field is given in Fig. 2.6. The figure matches with the general trend of velocity profile found in jets. The vorticity analysis in Fig. 2.6 also shows clockwise and anti-clockwise vorticies on the upper and lower boundaries of the jet which is also a distinct characteristic of a jet.

This validates the choice of cross correlation analysis and proves MATPIV to be effective for velocity vector calculation.

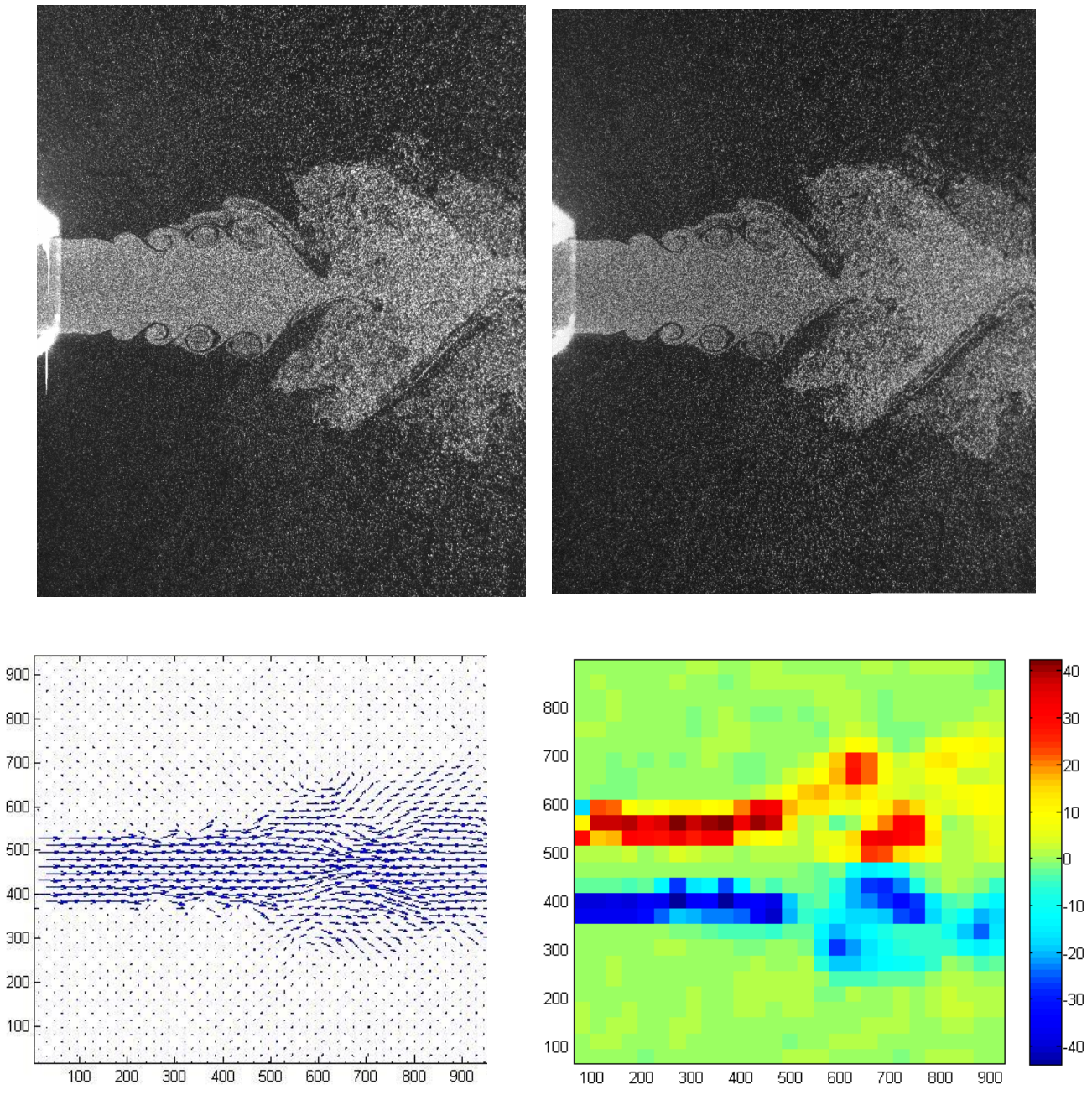

Fig. 2.6: PIV analysis of the test image. (Ref. : idtpiv.com)

2.7 Visualization of Microscopic Seed Particles

Visualization of the seed particles mixed with the continuous phase (water) is very important for proper velocity measurements of the continuous phase around the dispersed phase. Sometimes speckle patterns appear which can be mistaken as particles and result in 'bad vector' generation. The seed particles used are microscopic and of mean diameter of 8-12 μm as per Table 2.1. The resolution of the optical setup is set to 4.29 μm. A glass sheet is sprinkled with the particles on right side and the left side remaining un-sprinkled to compare images of both sides and understand any development speckle pattern. A hologram is digitally recorded. The reconstructed image given in Fig. 2.7(b) clearly shows particles on the right side of the glass sheet. In Fig. 2.7(c) the zoomed view is shown where the red circles are around single particles and the blue circles are around particle clusters. No speckles are observed in the un-sprinkled zone except few spots which are found as marks in the glass sheet, as the same pattern appears again and again in the same position of every image. This validates the particle viewing capability of the setup developed.

2.8 Resolution of the Optical Setup

Optical resolution describes the ability of the imaging system to resolve details in the object that is being imaged. The resolution measurement is very necessary in order to make sure whether the imaging system is capable of resolving the finer details of the measurement volume. The smallest objects in the measurement volume are seed particles which are of order 8μm and hence the resolution capability of the optical setup should be less than 8μm to properly resolve the seed particles and also accurate measurement of velocity.

The resolution is measured by 1951 USAF resolution test chart. 1951 USAF is a resolution test pattern conforming to MIL-STD-150A standard, set by US Air Force in 1951. The MIL-STD-150A pattern consists of six groups in three layers of patterns. The layer containing the bars with larger dimensions is located on the outer sides and the smaller layers repeat the same pattern but merge towards the center progressively. A total of twelve groups are there, numbered from -2 to 9. Each group has six elements numbered from 1 to 6. The smallest bar that can be resolved clearly indicates the resolution of the system.

Resolution is given by

$$\text{Resolution (lp/mm)} = 2^{\text{Group}+(\text{element}-1)/6} \tag{2.11}$$

Often a lookup table is generally used to calculate the resolution after the group and element number of the smallest visible bar in the image is known. The table is attached below in Table 3 and Table 4.

A hologram of the USAF 1951 is digitally recorded using the optical setup and then reconstructed to obtain an image of the resolution test chart. The image is zoomed to visualize the smallest possible bars that can be resolved. The smallest possible bars that can be resolved is element 6 and group 6 which gives a resolution of 114 Lp/mm or 4.39 μm. Hence the optical setup is able to resolve objects as small as 4.39 μm and the smallest object present in the test section is 8 μm. This is shown in Fig. 2.8 and Fig. 2.9.

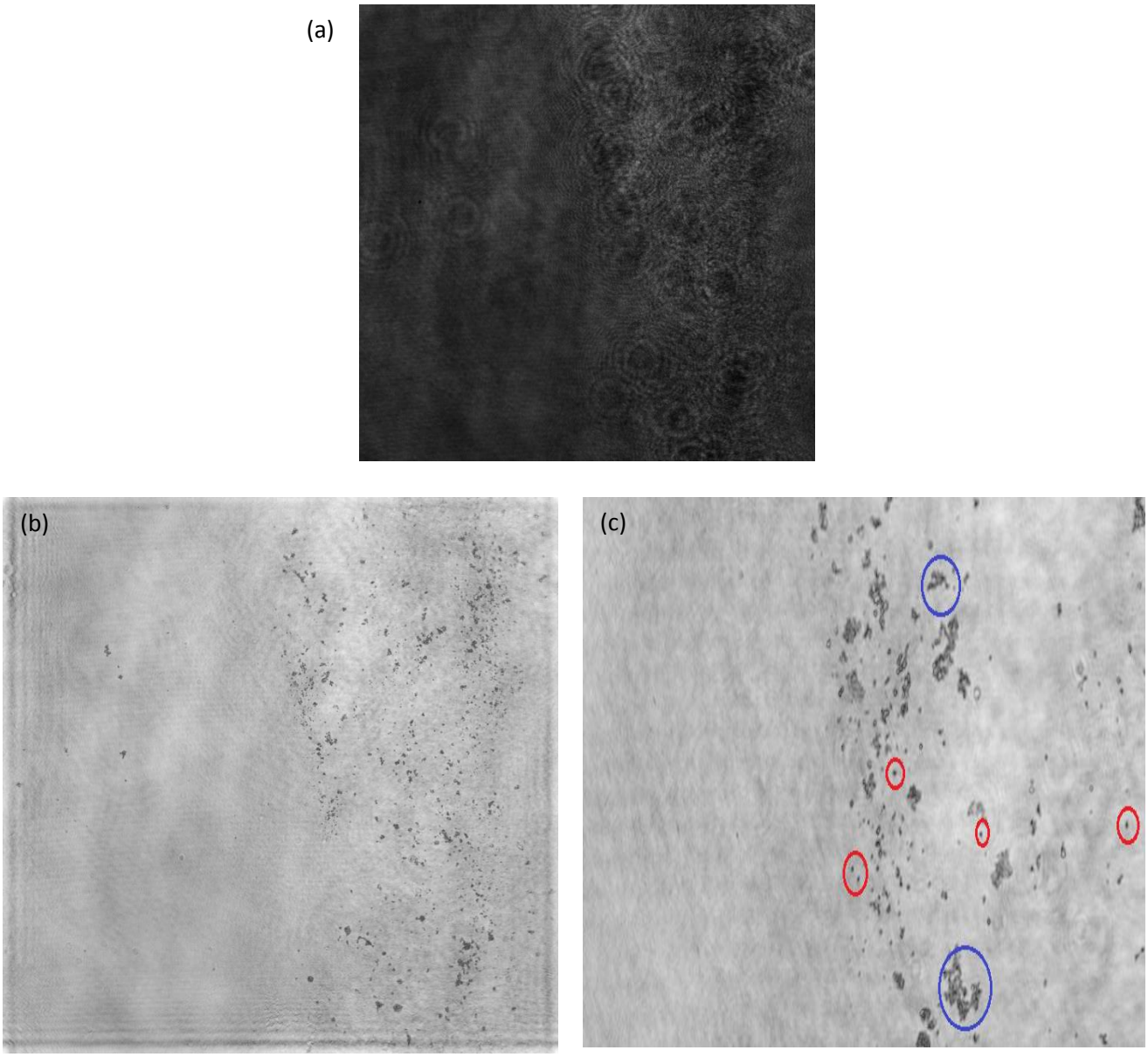

Fig. 2.7: (a) Hologram of a glass sheet sprinkled with seed particles. (b) Reconstructed image. (c) Zoomed view: red circles are for individual particles and blue circle for particle cluster.

2.9 Stability check of the system

2.9.1 Spatial frequency requirements

Photographic emulsions used in optical holography generally have resolution of 5000 Lp/mm. With this high resolution they are able to record holograms having a large angle between the object wave and the reference wave. The maximum spatial frequency that the system can resolve is given by

$$f_{\max} = \frac{2}{\lambda}\sin\frac{\theta_{\max}}{2} \tag{2.12}$$

In case of digital holography the maximum resolvable spatial frequency is given by

$$f_{\max} = \frac{1}{2\Delta x} \tag{2.13}$$

Where Δx denotes the distance between the neighboring pixels of the CCD, which in case of pco2000 is 7.8 µm. From Eq. (2.13) the maximum resolvable spatial frequency is in the range of 64.10 Lp/mm. This shows that the spatial frequency resolution of the optical setup is limited by the distance between the pixels of the CCD sensor. Combining Eq. (2.12) & (2.13) the angle (θ_{max}) becomes

$$\theta_{\max} = 2\arcsin\left(\frac{\lambda}{4\Delta x}\right) \approx \frac{\lambda}{2\Delta x} \tag{2.14}$$

The approximation is only valid for small angles. From Eq. (2.14), the maximum angle between the reference wave and the object wave, which is possible for the optical setup used in this experiment, is 0.34° and the angle used in this experiment is nearly 0°. This validates the spatial frequency requirements of the optical setup.

2.9.2 Stability against vibration

Variations in the optical path difference of the object and reference beams results in the movement of fringes and reduction in optical contrast of the hologram. The recorded hologram appears flat with low modulation. Variations as small as 1/10th of a wavelength can cause these disturbances. The setup for this experiment is mounted on an anti-vibrational table and pulsed laser is used to prevent errors due to vibration.

2.9.3 Minimum distance criteria for holography

The maximum angle between the rays emitted from an object of side L and the opposite side of CCD sensor of length NΔx is given by:

$$\theta_{max} \approx \frac{x}{d_{min}} = \frac{\sqrt{\frac{5}{4}}(L + N\Delta x)}{d_{min}} \tag{2.15}$$

The minimum object distance is given by

$$d_{min} = \sqrt{\frac{5}{4}}\frac{2\Delta x}{\lambda}(L + N\Delta x) = \sqrt{5}\frac{\Delta x}{\lambda}(L + N\Delta x) \tag{2.16}$$

Taking bubble diameter of 2 cm the minimum distance comes out to be 14 mm. In this setup the object distance from CCD is 5 cm which is more than the minimum distance calculated, and hence it satisfies the minimum distance criteria.

Table 2.3: Chart for resolution measurement (in Lp/mm) with group and element number.

Number of Line Pairs / mm in USAF Resolving Power Test Target 1951												
Group Number												
Element	-2	-1	0	1	2	3	4	5	6	7	8	9
1	0.250	0.500	1.00	2.00	4.00	8.00	16.00	32.0	64.0	128.0	256.0	512.0
2	0.280	0.561	1.12	2.24	4.49	8.98	17.95	36.0	71.8	144.0	287.0	575.0
3	0.315	0.630	1.26	2.52	5.04	10.10	20.16	40.3	80.6	161.0	323.0	645.0
4	0.353	0.707	1.41	2.83	5.66	11.30	22.62	45.3	90.5	181.0	362.0	-----
5	0.397	0.793	1.59	3.17	6.35	12.70	25.39	50.8	102.0	203.0	406.0	-----
6	0.445	0.891	1.78	3.56	7.13	14.30	28.50	57.0	114.0	228.0	456.0	-----

Table 2.4: Chart for width of 1 line (in micrometer) with group and element number.

Width of 1 line in micrometer in USAF Resolving Power Test Target 1951												
Group Number												
Element	-2	-1	0	1	2	3	4	5	6	7	8	9
1	2000.00	1000.00	500.00	250.00	125.00	62.50	31.25	15.63	7.81	3.91	1.95	0.98
2	1785.71	891.27	446.43	223.21	111.36	55.68	27.86	13.89	6.96	3.47	1.74	0.87
3	1587.30	793.65	396.83	198.41	99.21	49.50	24.80	12.41	6.20	3.11	1.55	0.78
4	1416.43	707.21	354.61	176.68	88.34	44.25	22.10	11.04	5.52	2.76	1.38	-----
5	1259.45	630.52	314.47	157.73	78.74	39.37	19.69	9.84	4.90	2.46	1.23	-----
6	1123.60	561.17	280.90	140.45	70.13	34.97	17.54	8.77	4.39	2.19	1.10	-----

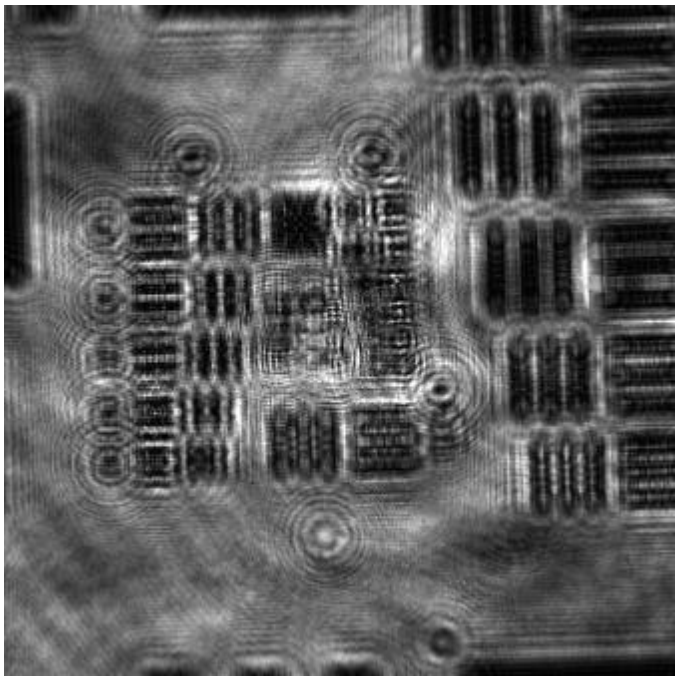

Fig.2.8: A hologram of USAF 1951.

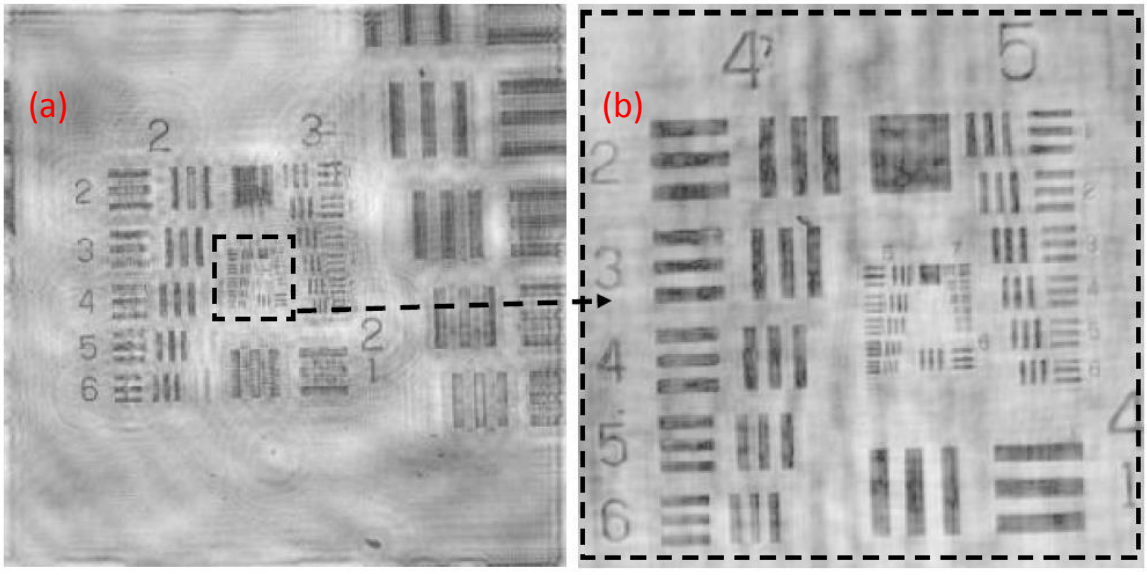

Fig. 2.9: (a) Reconstructed image of the hologram in Fig. 2.8.

(b) Enlarged view of the dotted area in (a).

CHAPTER III

RESULTS AND DISCUSSION

3.1 Introduction

This chapter presents results obtained by the developed experimental setup with discussion on the techniques of measurement and comparison with theoretical and measured results. The position measurement ability of the setup is analyzed where a correlation is developed to predict the position of the object. The experimental results are compared with theoretical calculations and measurements with an engineering ruler. The size measurement technique is discussed and measurements are compared with that of a screw gauge. The dispersed phase measurements are done by the size measurement technique. After position and size measurements the variations in the reconstructed image quality is studied for different distances (dr) between the CCD and point source of light.

The reconstructed images obtained from the holograms are not suitable for the software to process for velocity vectors. This leads to the generation of erroneous velocity vectors. To prevent this the images are processed using different techniques which is elaborated.

Lastly the velocity measurements are discussed with measurements for both the continuous and dispersed phase.

3.2 Measurement of particle position

In holographic microscopy the object distance in recording is different from the object distance in reconstruction. This hinders accurate prediction of the object position. Hence a correlation is developed to predict the real object distance from the object position obtained in reconstruction. This is done using a USAF 1951 target. The test target is placed at different known distances in between the point source of the beam and the CCD sensor and holograms are recorded for each of the position. These recorded holograms are then reconstructed and the position of the focused image is noted. A list of values of reconstructed distance corresponding to the real object distance is given in Table 1. The correlation developed from the data is given below and plotted as shown in Fig. 3.1

$$\mathbf{y = 15.548x^2 - 342.87x + 2125} \tag{3.1}$$

where y represents the reconstructed distance in mm and x represents the real distance in cm.

A theoretical analysis of the reconstructed object distance is also done. According to the theory of Fourier transform among Δx, Δy, Δν and Δμ the following relationship exists

$$\Delta\nu = \frac{1}{N\Delta x}; \qquad \Delta\mu = \frac{1}{N\Delta y} \tag{3.2}$$

After re-substitution

$$\Delta\xi = \frac{\lambda d}{N\Delta x}; \qquad \Delta\eta = \frac{\lambda d}{N\Delta y} \tag{3.3}$$

With consideration of different reconstruction distance from object distance this can be written as

$$\Delta\xi' = \frac{\lambda d'}{N\Delta x} \quad ; \quad \Delta\eta' = \frac{\lambda d'}{N\Delta y} \tag{3.4}$$

The resolution measured in the position of the test section is 4.29 μm. Keeping the required resolution ($\Delta\xi$) at 4.29 μm, with a pixel size (Δx) of 7.8 μm, taking wavelength of the coherent beam (λ) of 532 nm and with 2048 pixels, the real object distance is calculated to be 128.8 mm, which gives a reconstructed distance of 288mm as per the correlation developed. The reconstruction distance originally comes to be 289mm while reconstructing the bubble images with an error of 0.3% for the correlation prediction at the position of the rising bubbles is calculated.

3.2.1 Determination of position of bubble and walls

After the reconstruction of the hologram, the plane containing the focused bubble image is generally observed manually by choosing between the images reconstructed at different positions. The manual technique is subject to human error and hence a technique is developed to choose the best plane for the bubble. It is done by 'color fill' mode of Sigma Scan software where the inbuilt algorithm fills a designated color inside the nearest closed boundary. When the bubble is best focused the color remains inside the bubble only as the boundaries of the bubble is sharp. Whereas in other planes of reconstruction the bubble is not well focused and hence the bubble boundary is broken, so the color fills spaces outside the bubble. This is demonstrated in Fig. 3.2. The reconstructed distance of the best plane of bubble comes out to be 322 mm which is then converted to real object distance by using the correlation in Eq. (3.1) and is 134 mm. The position measurement capability of the system is further tested by measuring the wall position. A hologram is recorded for air bubbles attached to both the walls as shown in Fig. 3.3. The hologram is then reconstructed to find the best planes for the bubble attached with front and rear walls,

Table 3.1: Values of real, reconstructed and correlation predicted distances of the object from CCD with error percentage.

Distance from CCD (in cm)	Reconstructed distance (in mm)	Correlation distance (in mm)	Error (%)
10	206	251.1	21.8
11	243	234.7	3.4
12	296	249.4	15.7
13	327	295.3	9.6
14	399	372.2	6.7
15	470	480.2	2.1
16	566	619.3	9.4
17	686	789.5	15
18	1090	990.8	9

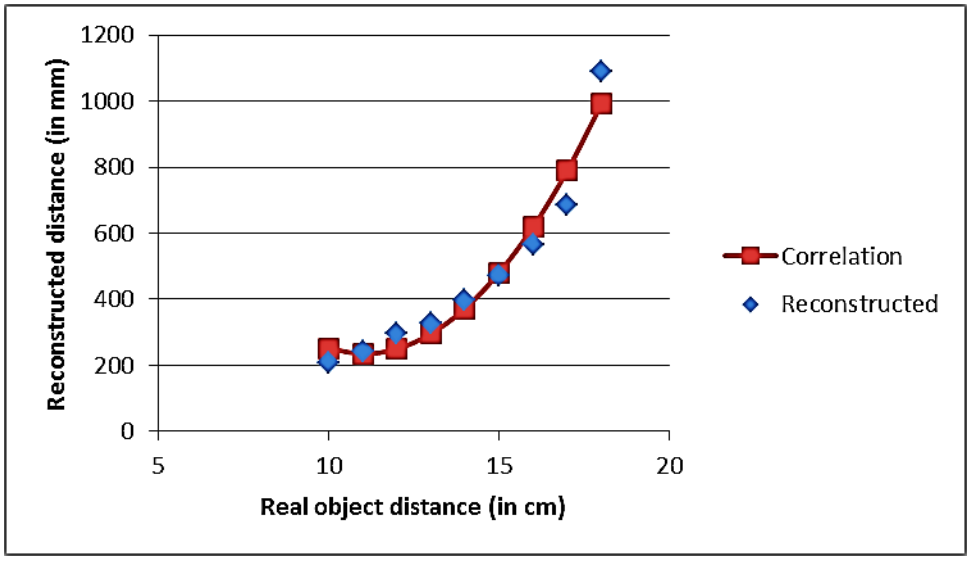

Fig. 3.1: A plot of the reconstructed distance and the predicted distance by correlation.

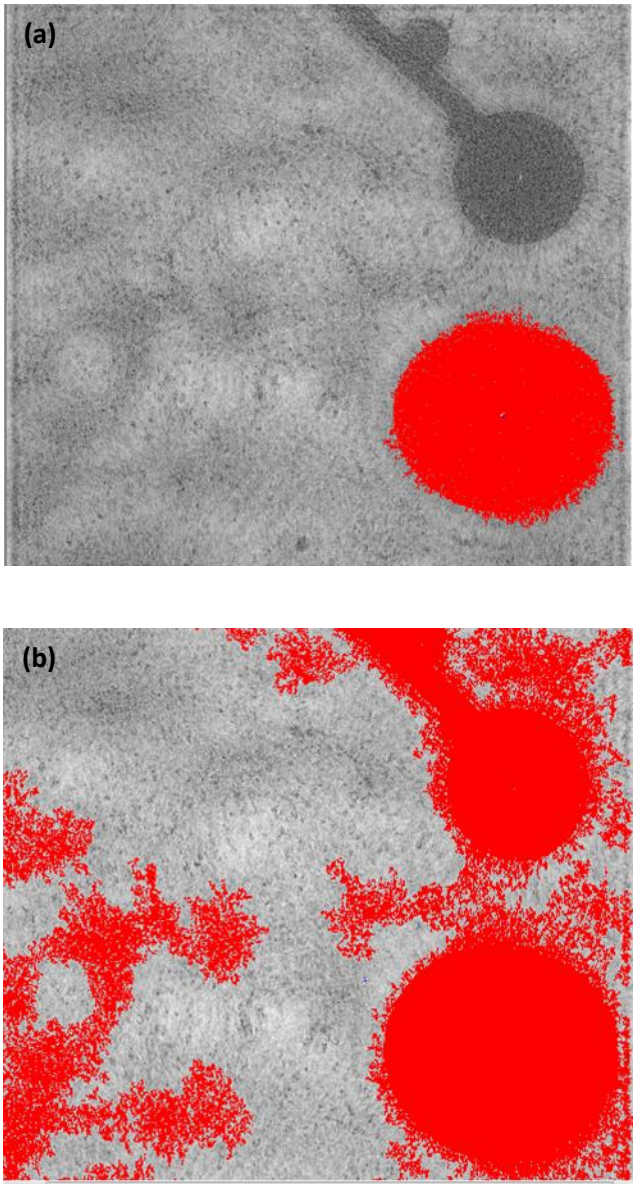

Fig. 3.2 (a) Sigma Scan 'fill mode' applied to the best plane of bubble.

(b) Sigma Scan 'fill mode' applied to an unfocused plane of bubble.

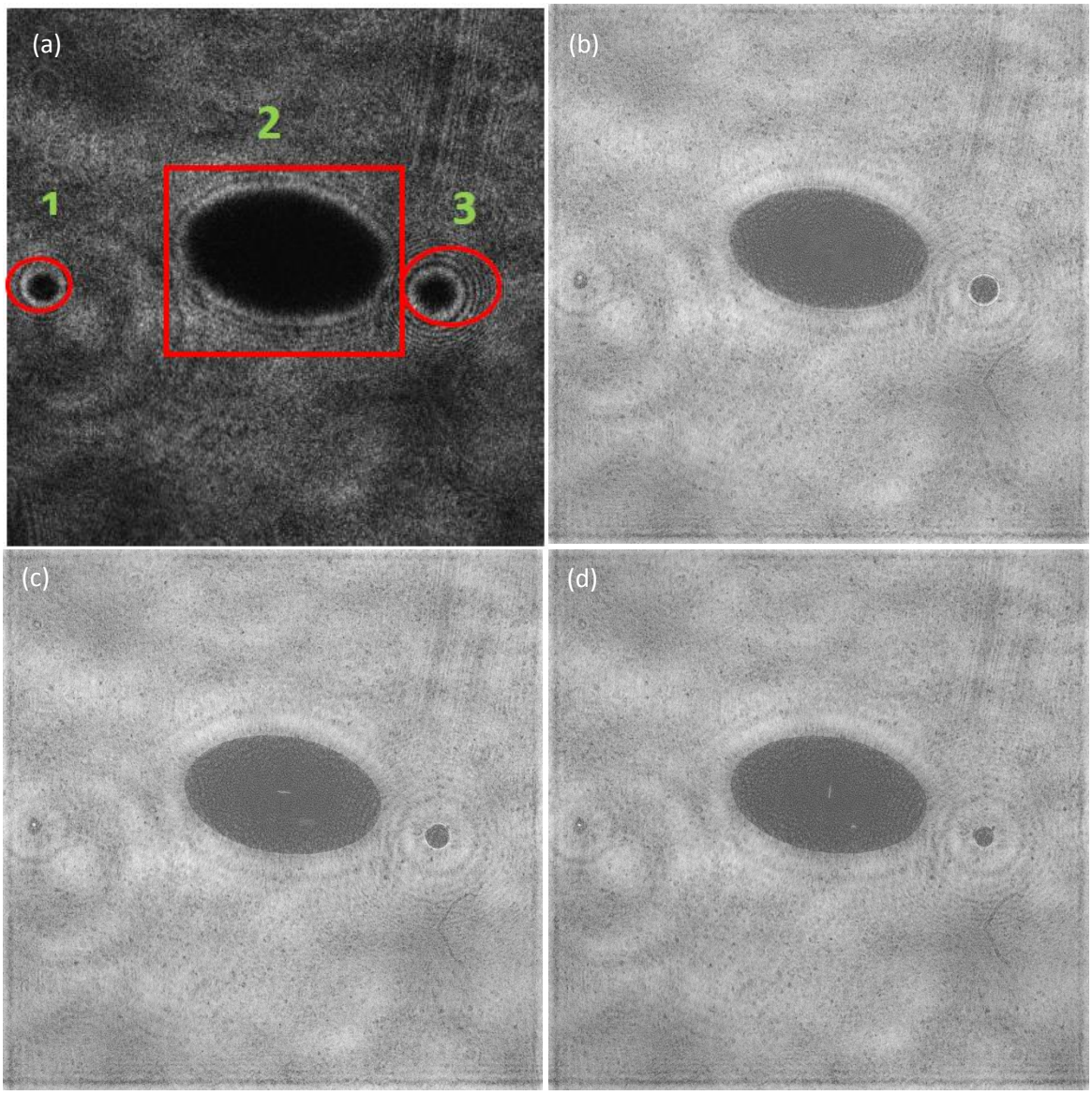

Fig. 3.3 (a) Hologram showing bubbles attached to the front and rear wall and bubble rising in the middle. (b) Reconstructed hologram at 289mm. (c) Reconstructed hologram at 322mm. (d) Reconstructed hologram at 359mm.

which are 281mm and 359mm respectively and recorded as the reconstruction position of the walls. Using the correlation developed the position of the walls are found out to be 127 mm and 139 mm. The actual measured position using an engineering ruler is found out to be 110mm and 135mm hence the error is found to be 15.4% and 2.9%.

3.3 Measurement of dimensions

The injector needle has a diameter of 0.279 mm as measured in screw gauge with least count of 0.025 mm. The width of the image of injector is noted in pixels. The pixel width is then compared with the width in mm and pixel to mm conversion scale is developed as given below

Millimeter: Pixel =1: 286. (3.5)

3.3.1 Measurements of the dispersed phase

Using this conversion scale the average for the major and minor axis of the bubble is calculated over 50 images. Other parameters of the bubble like area, center co-ordinates, etc. are calculated. A list of the dispersed phase measurements is given in Table 2.

3.4 Area of Measurement

From the conversion scale given in Eq. (3.5) and taking in account 2048 pixels on both sides of the CCD sensor, the area of measurement is calculated as 7.16mm X 7.16mm.

3.5 Variation of the image quality with ‘dr’

The ‘dr’ is distance between the point source of the beam and the CCD sensor. This is used by convolution approach to reconstruct the hologram. The dr in this experiment is 240 mm which is

measured by an engineering ruler with least count of 1 mm. The variation of the reconstructed image with dr is analyzed to understand the requirement of precise measurement of dr. It is found that the image does not vary with minor fluctuations in dr of order of 10 mm. The quality of the image remains the same as demonstrated in Fig. 3.4.

3.6 Image processing

The reconstructed image obtained from the hologram cannot be used for velocity measurement. Image processing is needed to reduce optical errors, speckles and in a way enhance the image to make it easy for the software to process the data and lead to accurate results. An image obtained from reconstruction of hologram generally has more noise compared to a typical PIV image where particles appear as bright dots on dark background. Fig. 3.5 shows two images of bubble rising in seeded water, but one recorded with a PIV setup and another with a holography setup. The image processing is done through several steps.

3.6.1 Averaging of holograms and Reconstruction

All the holograms recorded for the test setup are averaged with equal weightage. The resulting hologram obtained is reconstructed throughout the measurement volume, using convolution approach, to obtain images at different position.

3.6.2 Image Subtraction

A desired hologram is reconstructed throughout the measurement volume at every millimeter. Each image at a certain position is subtracted by the averaged image for that position. The subtraction is done for all the images throughout the measurement volume.

Table 3.2: Measurements of the dispersed phase.

Averaged Measurements	In pixels	In mm
Area of the bubble	373789	1306.9
Length of major axis	783.3	2.7
Length of minor axis	720.5	2.5
Perimeter	25738.7	89.9
x-co-ordinate of center	1374	4.8
y-co-ordinate of center	1629	5.6

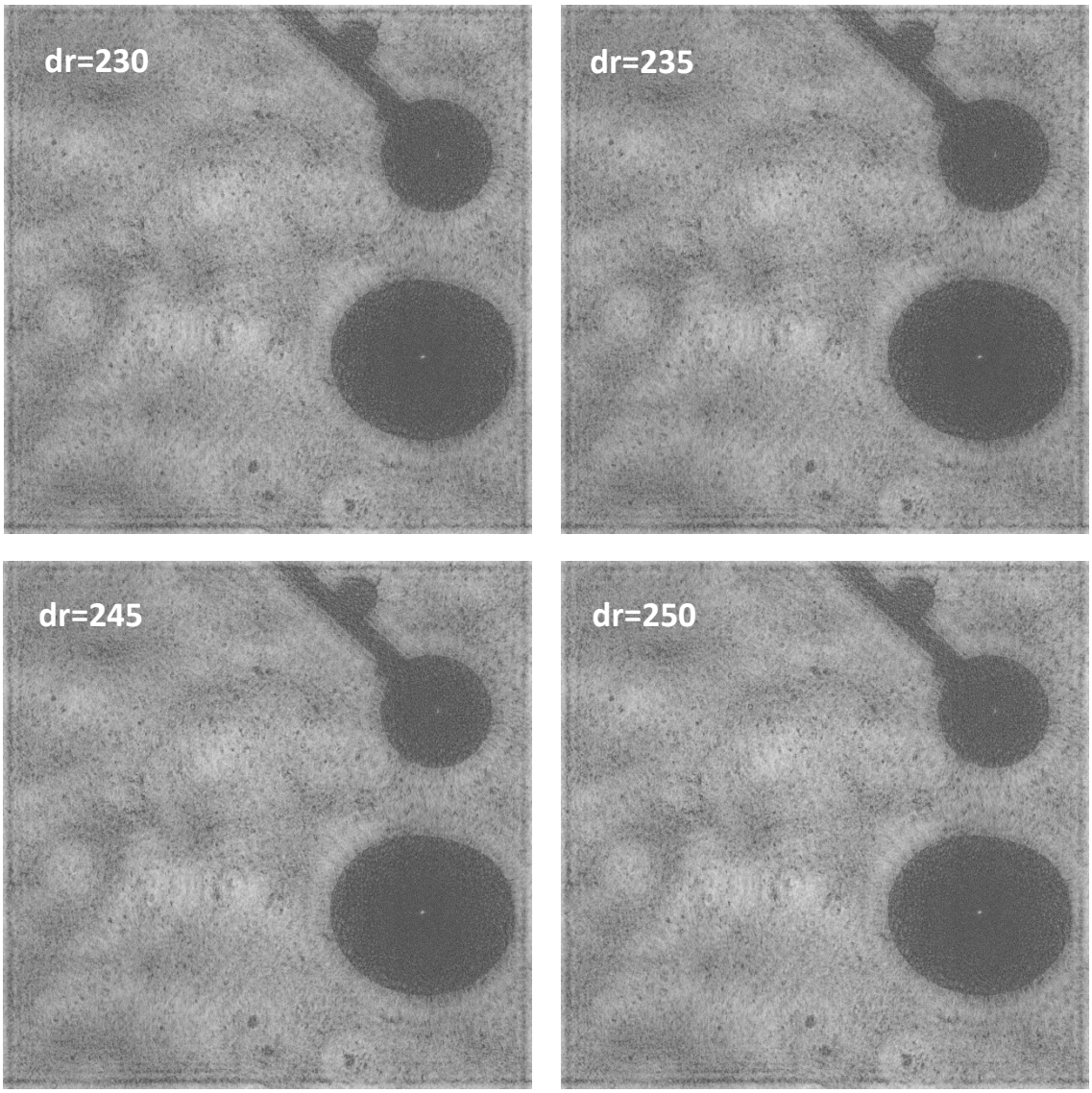

Fig. 3.4: Reconstructed image with different 'dr' distances. This shows minor fluctuations in 'dr' does not affect the image.

(a)

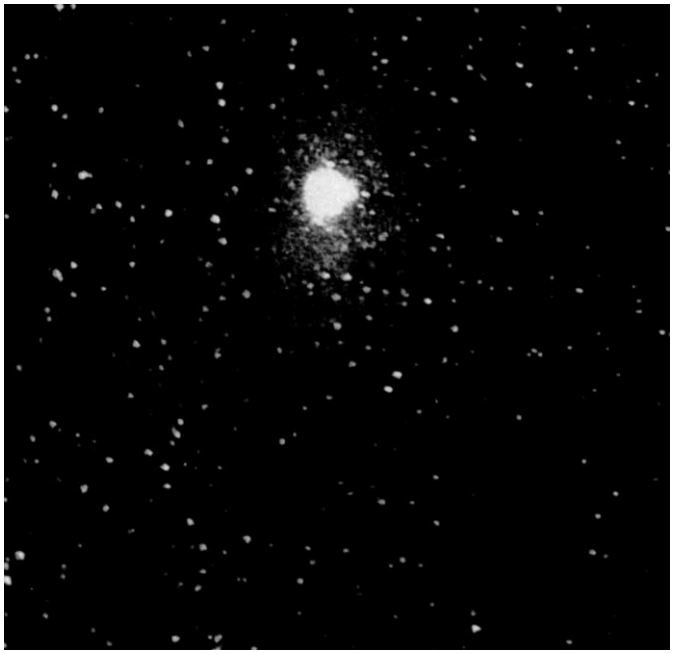

(b)

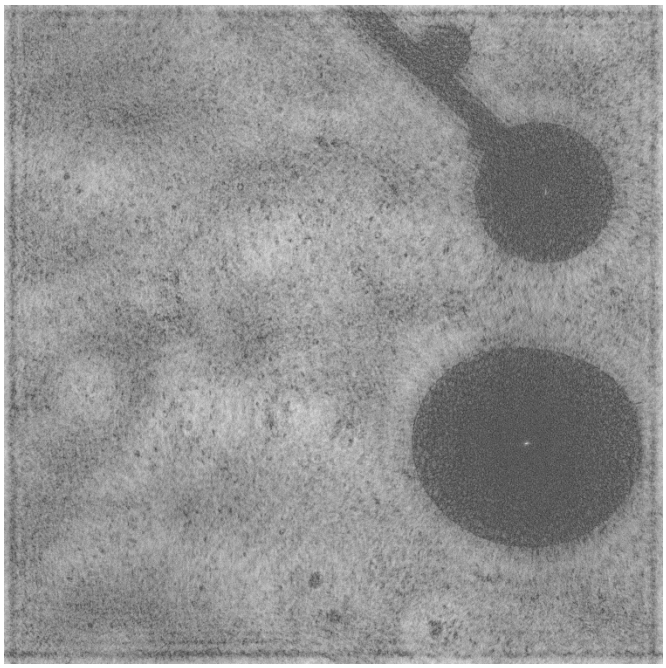

Fig. 3.5: (a) Raw PIV image.

(b) Reconstructed image from hologram.

3.6.3 Image Inversion & thresholding

The resulting image from the above step is first inverted and then thresholded to result in PIV like image, having seed particles as bright dots on a dark background.

Finally an image of PIV quality is achieved which is ready for cross-correlation analysis to give velocity vectors for the continuous phase. The image processing flow chart is given in Fig. 3.6.

3.7 Calculation of velocity vectors

Velocity vectors are calculated for both the continuous and dispersed phase following different methodologies.

3.7.1 Continuous phase

After obtaining a filtered image, which is intensity thresholded and containing only the seed particles, it is processed for continuous phase velocity field. It is done using open source MATLAB toolbox, MATPIV. This toolbox provides different schemes to conduct single or multiple pass PIV. Multiple pass cross correlation is used to calculate the velocity vectors from the image pair. The image $I_1^{i,j}$ is cross correlated with $I_2^{i,j}$ as follows

$$R(s,t) = \sum_{m=0}^{M-1} \sum_{n=0}^{N-1} [. I_1^{i,j}(m,n). I_2^{i,j}(m-s, n-t)] \quad (3.6)$$

where i, j represents the row and column of the sub window in the image pairs. Input to the program are the two images to be cross-correlated in the order of the images being captured, the choice of interrogation window size, the time delay between the two frames, the percentage of overlapping of the windows and the number of pass needed.

The syntax for the input is given below

[x, y, u, v] = matpiv ('Image 1', 'Image 2', IW, Δt, % of overlapping, 'no. of passes') (3.7)

where x, y are positions and u, v are velocities, Image 1 is the first image recorded and Image 2 is the second image recorded by the CCD. IW represents the interrogation window size; Δt represents the time delay between the frames recorded. The last two terms denotes the percentage of overlapping between the windows and the number of passes through which program is needed to be run respectively.

Finally after processing the values of x, y, u and v are stored in a matrix and plotted using vector plotting code. The plot with only the continuous phase is shown in Fig. 3.7. This step is repeated throughout the depth of the measurement volume which is chosen to be 4mm and given in Fig. 3.8.

The velocity map of the continuous phase shows some implausible velocity vectors on the left of the bubble, where two velocity vectors are almost at same position but they are in opposite directions. This is due to the fact that the cross correlation analysis produces instantaneous velocity vectors. Averaging of numerous velocity maps for same situations will eradicate these bad vectors from the map.

3.7.2 Dispersed phase

The dispersed phase has a larger displacement compared to seed particles between the two recorded frames. Hence the velocity obtained for the dispersed is average velocity. On cross correlating the velocities of the dispersed phase do not appears or in some cases produce faulty

results as the cross correlating scheme is for very small movements. To measure the velocity of the dispersed phase the center of the bubble is measured in both the frames from which the displacement of the bubble is measured. Using the time delay velocity of the dispersed phase is achieved. The velocity data is then plugged into the velocity matrix of the continuous phase and plotted. A plot of the velocity field of the dispersed phase is given in Fig. 3.9. A plot of both the phases is given in Fig. 3.10 and a measurement through the volume is shown in Fig. 3.11.

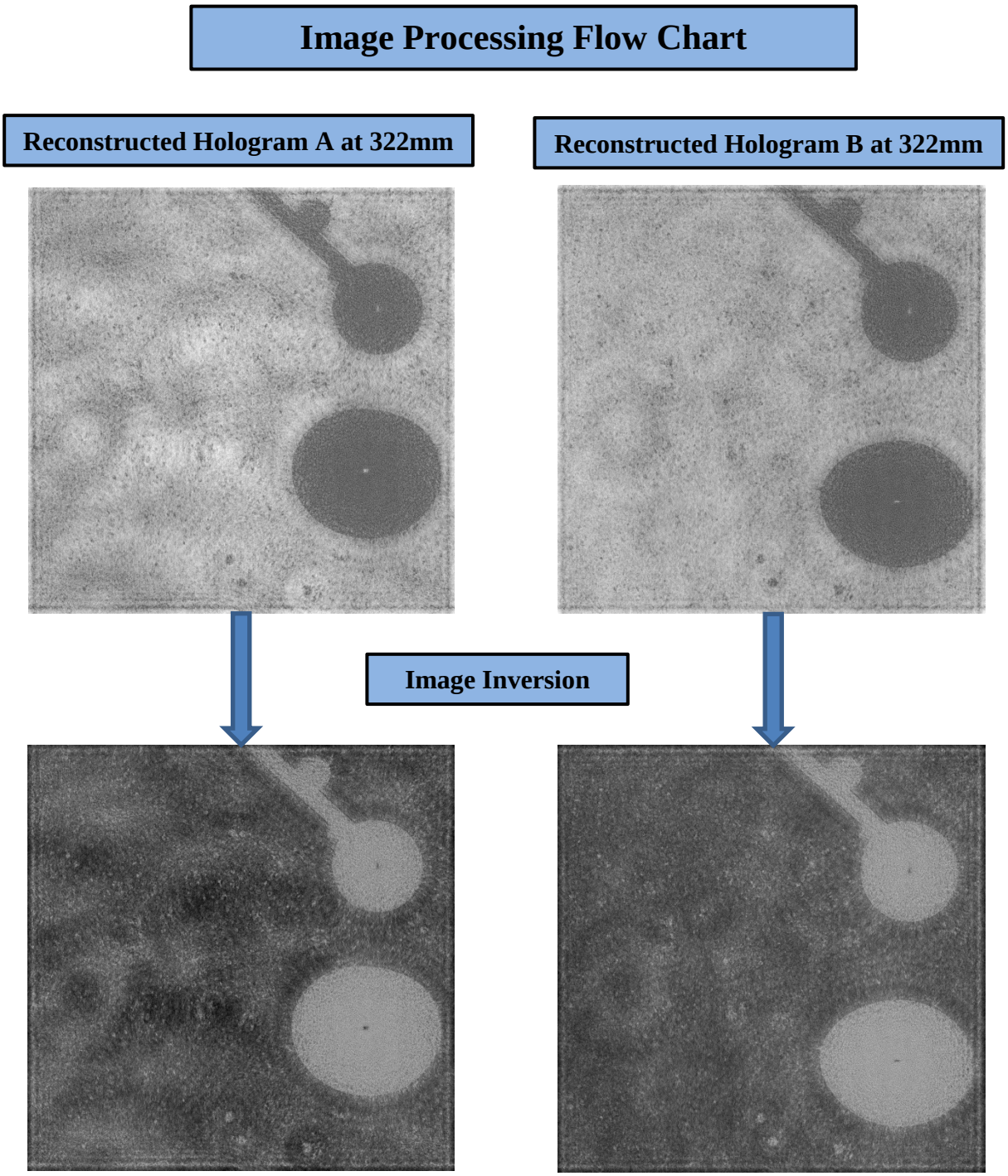

Fig. 3.6: Flow Chart of the Image Processing Scheme. (Continued in next page)

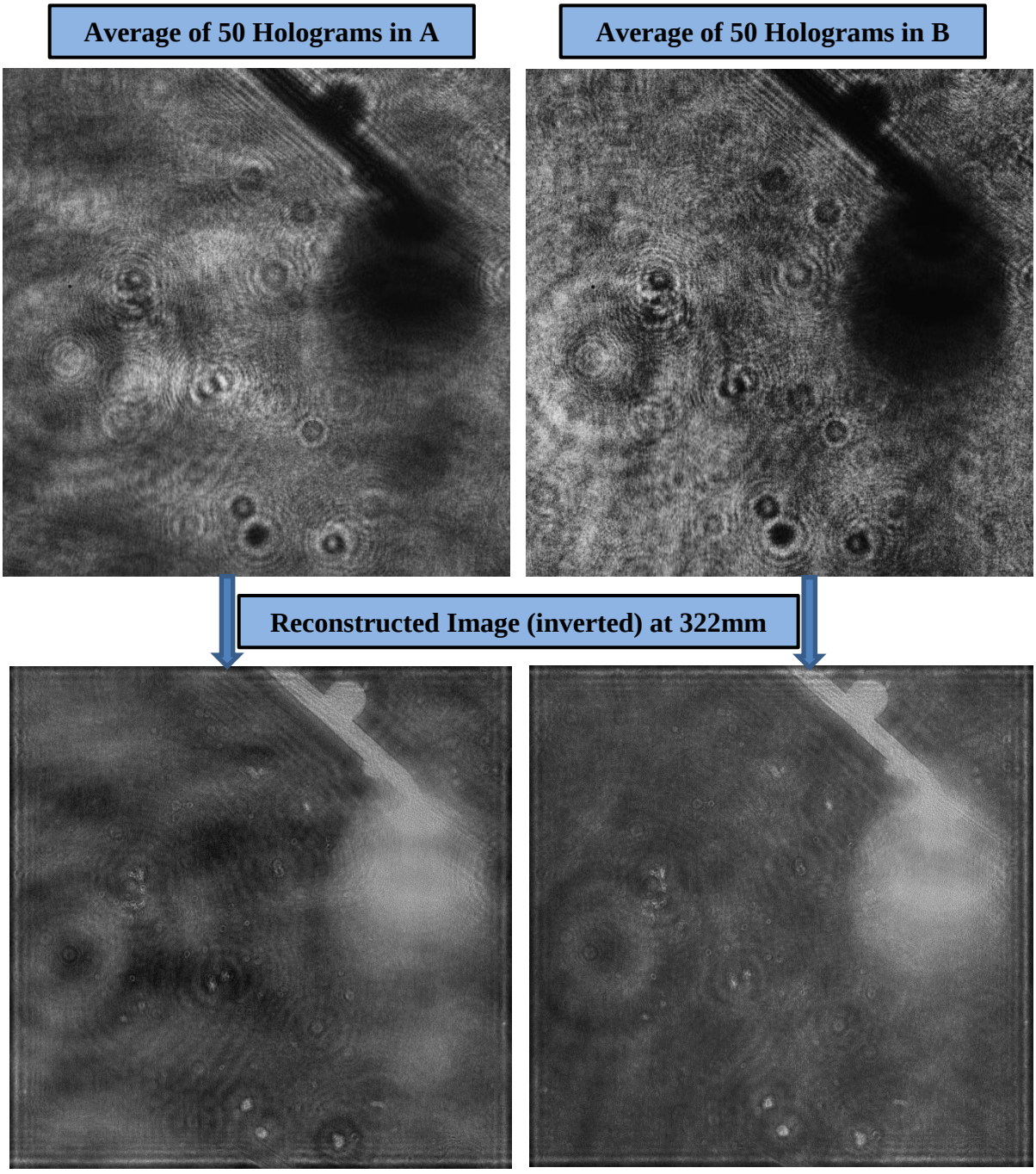

Fig. 3.6: Flow Chart of the Image Processing Scheme. (Continued in next page)

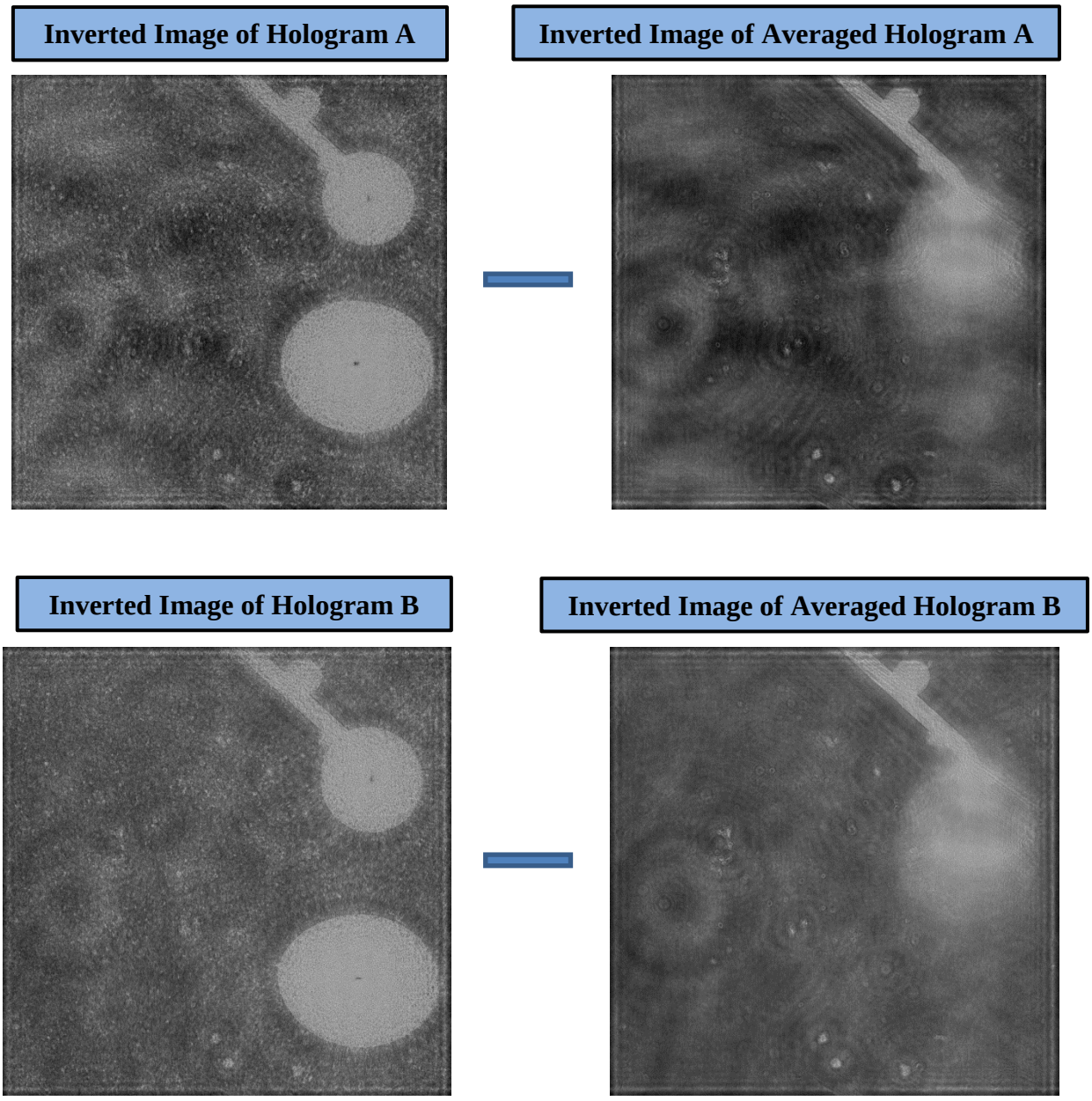

Fig. 3.6: Flow Chart of the Image Processing Scheme. (Continued in next page)

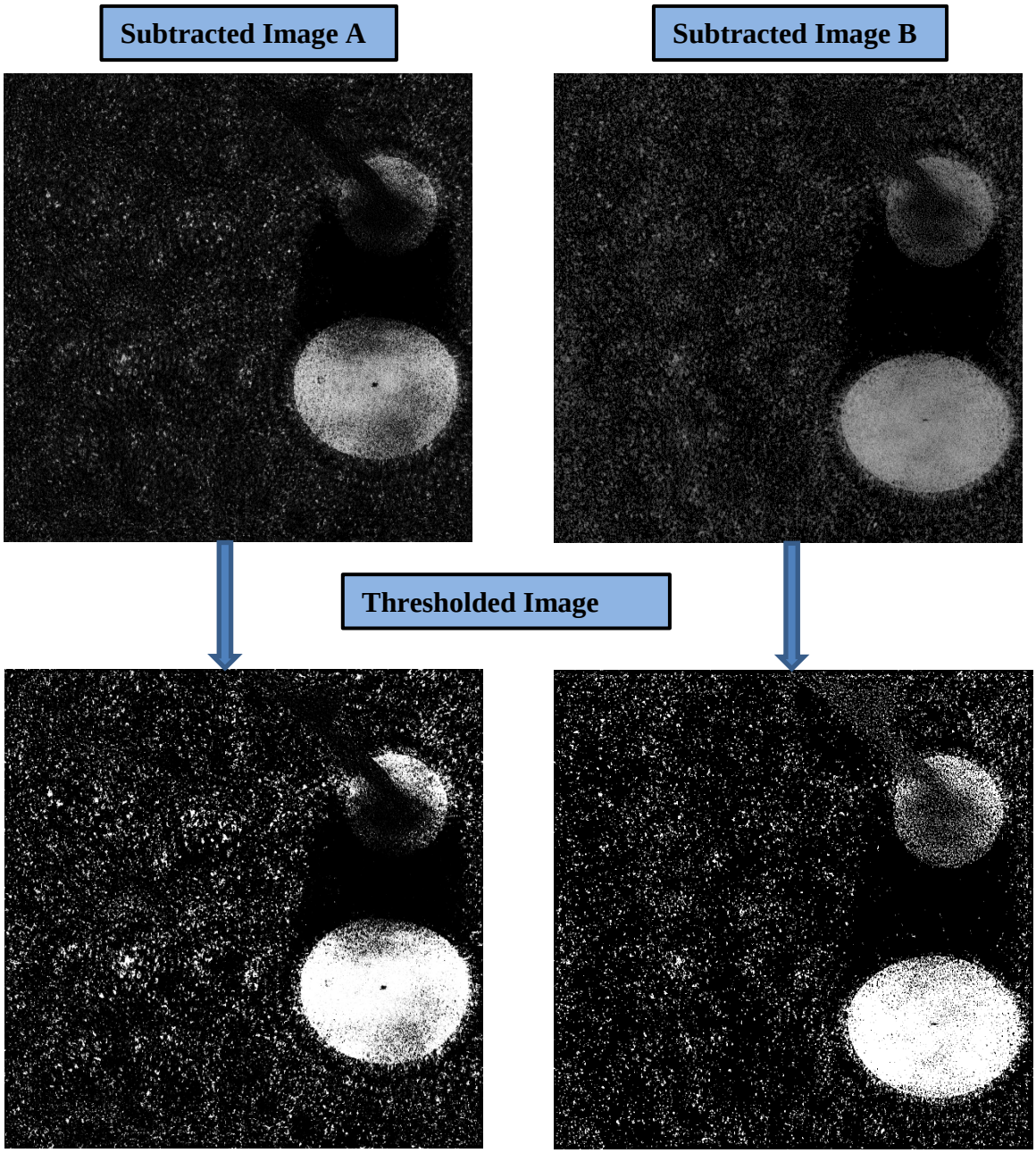

Fig. 3.6: Flow Chart of the Image Processing Scheme.

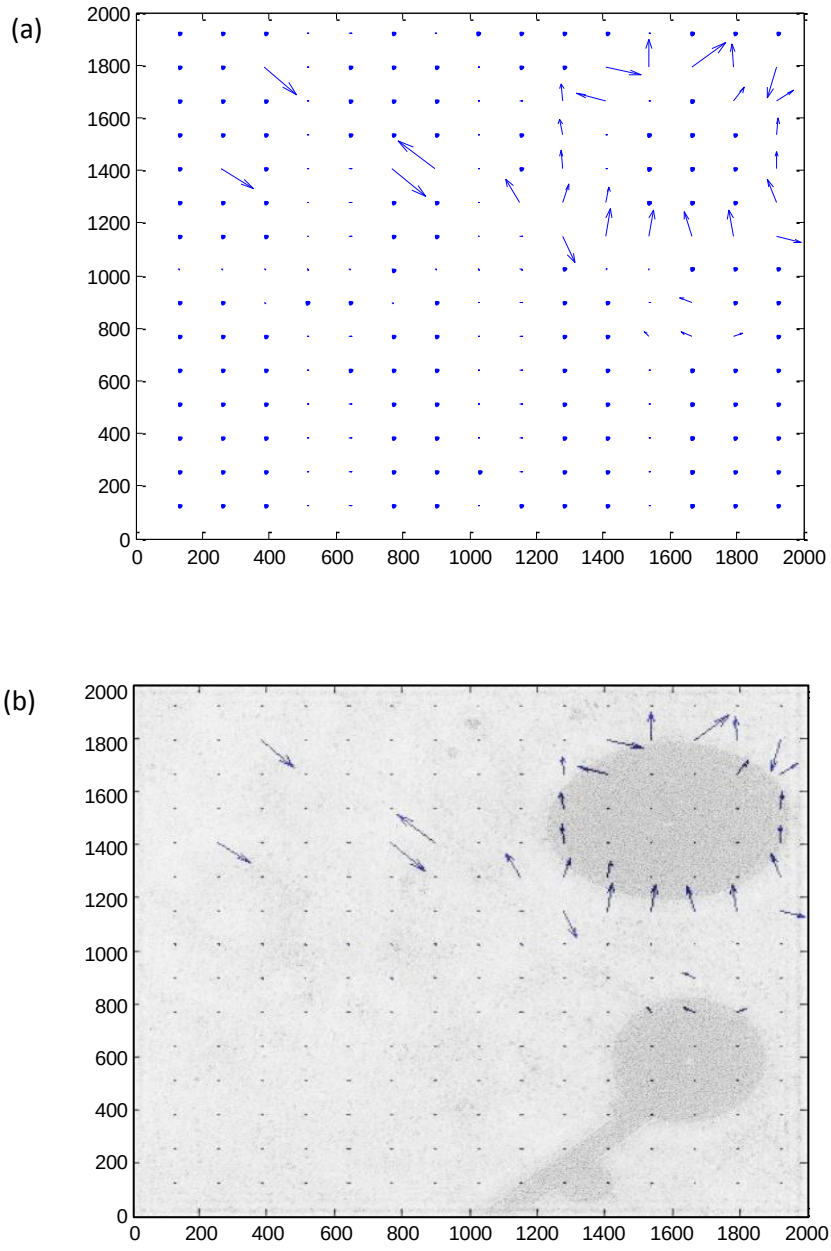

Fig. 3.7: (a) Velocity of the continuous phase around the bubble reconstructed at 322mm.

(b) Velocity vectors superimposed on the bubble image reconstructed at 322mm.

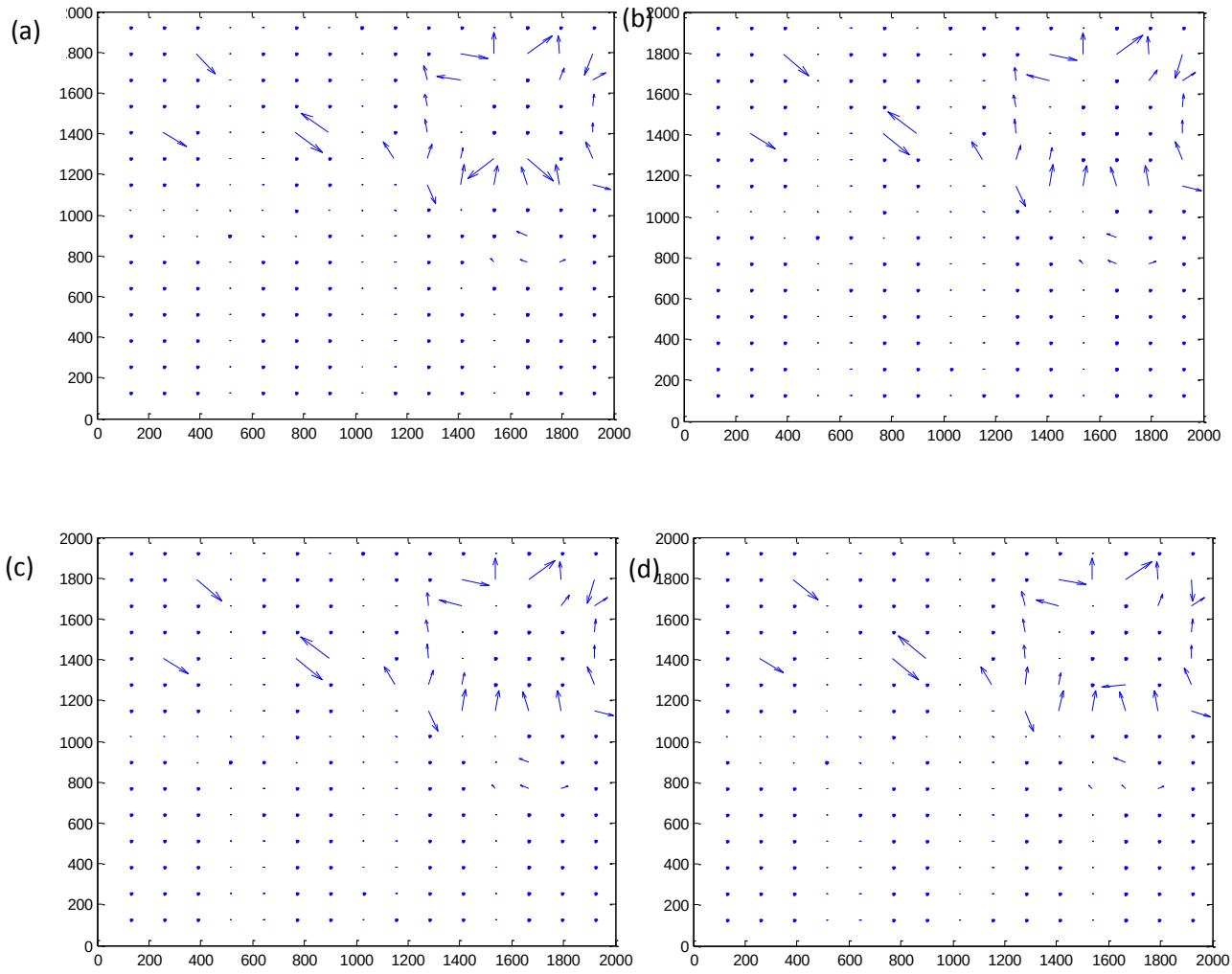

Fig. 3.8: Velocity vectors of the continuous phase at different reconstructed distances, (a) 320mm, (b) 321mm, (c) 322mm and (d) 323mm

.

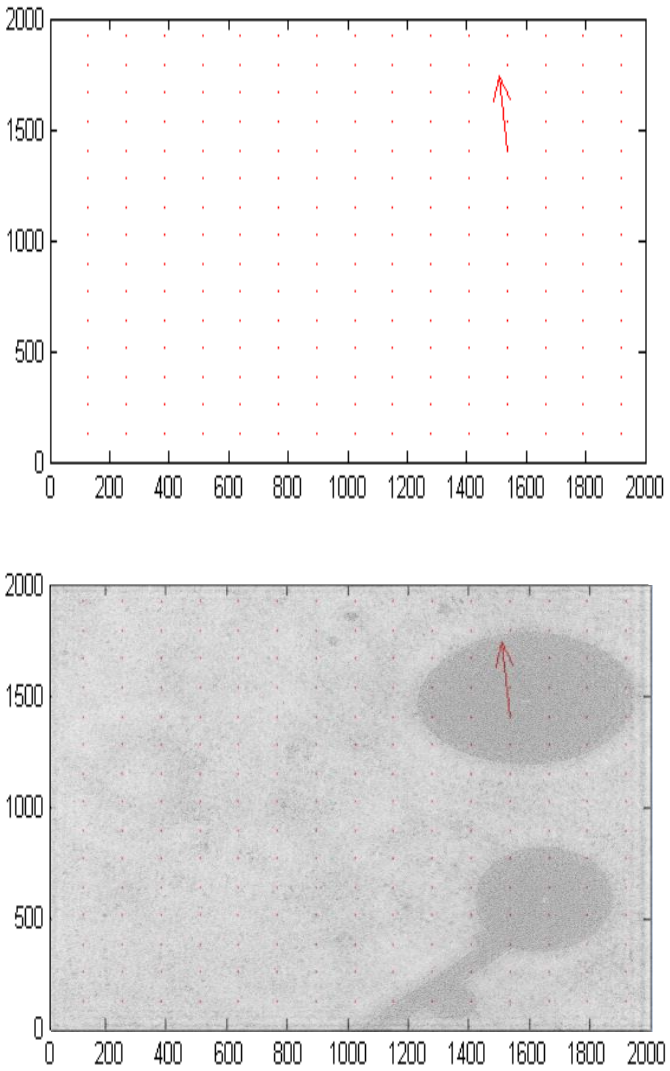

Fig. 3.9: (a) A plot of the dispersed phase velocity vector at the best plane of bubble (322mm).

(b) Velocity vectors superimposed on the bubble image reconstructed at 322mm.

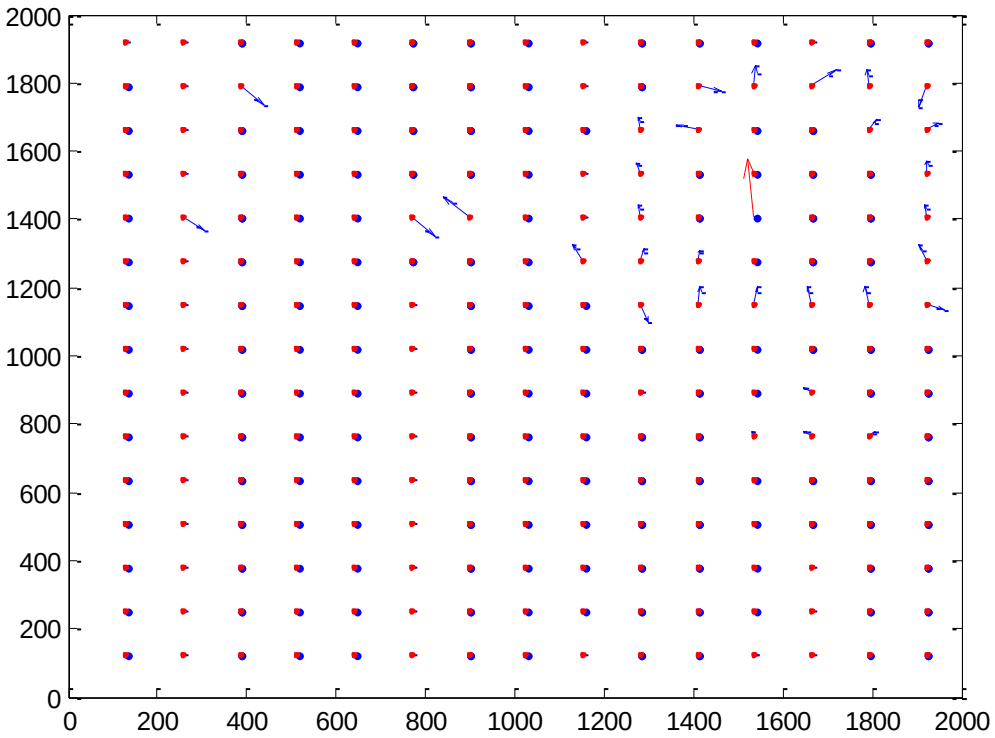

Fig. 3.10: A plot of both the dispersed and continuous phase at the best plane of bubble.

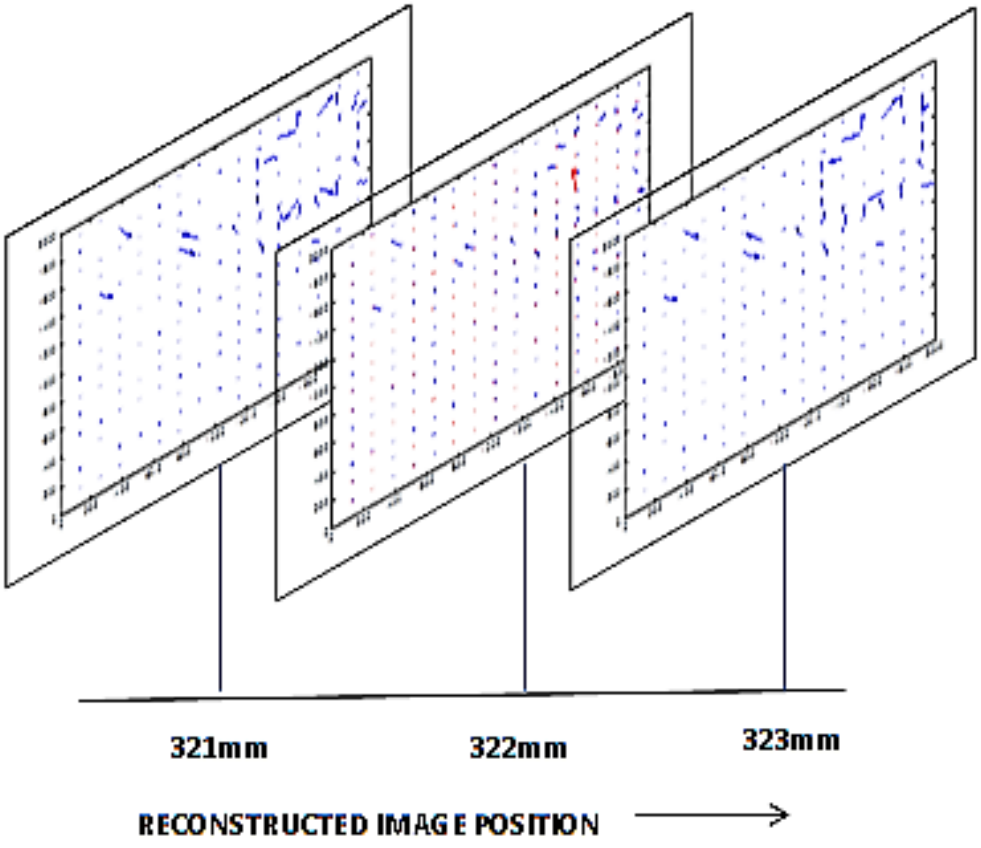

Fig. 3.11: Two component-three dimensional measurements (2C-3D).

CHAPTER IV

SUMMARY AND CONCLUSIONS

4.1 Summary

This study involved developing holographic setup for multiphase velocimetry. Introduction of holography in multiphase velocimetry will improve the three dimensional measurement as holography has the ability to store three dimensional information in two dimensional plane and hence can be more effective than the conventional stereo setup. Moreover holographic microscopy will enable to visualize phenomenon occurring in the microscopic world.

This is done by first calibrating the position and size measurement of the holographic microscopy setup. Holograms of the measurement volume are then recorded and images are reconstructed throughout the measurement volume. A technique of determining the focused image is also developed. The images obtained from reconstructing the holograms are noisy and not effective for velocity measurement. Hence, these images are then processed by subtracting the reconstructed image of the averaged hologram. Finally intensity thresholding is applied to amplify the seed particles and reduce the noise in the image.

The image pair recorded with a time delay is then cross correlated using the MATPIV scheme, which runs on MATLAB, to calculate the velocity field of the continuous phase. The bubble

velocity is separately calculated by measuring the difference in the movement of the center of the bubble and dividing it with the time delay. Hence velocities of both the phases are obtained

Finally the cross correlation algorithm is validated using test images with known results. This procedure can be extended throughout the test volume to calculate the two component three dimensional (2C-3D) velocity field for the test section.

4.2 Conclusions

The major conclusions of the present study are as follows.

1. A correlation is developed between the real object distance and the reconstructed object distance. By this position of the real position of the object can be predicted from the reconstructed distance at which the image of the object becomes focused.

2. A millimeter to pixel scale is developed from which dimensions of objects can be measured. This is used to measure the bubble diameter, area and center position.

3. A technique is developed to find the focused image plane. Using this manual technique of selecting the best plane of bubble is replaced by software analysis which facilitates better prediction of the focused image.

4. A technique of clearing the holographic image to make it suitable for velocity analysis is developed. This technique clears the background of the holographic image and projects only the focused seed particles and the bubble.

5. Velocity data of both the phases in the test section is measured.

4.3 Future works

The present study shows that holography can be applied to multiphase velocity measurements. The following are recommended for future works.

1. A better image processing scheme to properly visualize the wake region behind the bubble. A better scheme will ensure proper filtering of the image and hence generate detailed velocity vectors in the bubble wake region and will suppress bad vector generation.

2. A code to automatically detect the focused plane of the dispersed phase which will reduce processing time.

3. A cross correlation algorithm which will yield three component velocity map. The velocity measured are two component velocity maps, a three component velocity map will provide a better picture of the situation.

4. A stereo holographic setup which will improve the z direction resolution of velocity field. The technique used has a limitation of minimum reconstructed distance of 1mm but with stereo setup this can be reduced and will enable more accurate velocity measurements.

REFERENCES

Hariharan P., “Basics of Holography”. Cambridge University Press, (2002).

Brucker C., “Structure and dynamics of the wake of bubbles and its relevance of for bubble interaction”, Phys Fluids 11, 1781-1796, (1999).

Burke J., Hess C. and Kebbel V., “Digital holography for whole field spray diagnostics”, In: Proceedings of the 11th international symposium on applications of laser techniques to fluids mechanics, Instituto Superior Tecnico, Lisbon, Portugal, (2002).

Cheng Y., Pothos S. and Diez F. J., “Phase discrimination method for simultaneous two-phase separation in time resolved stereo PIV measurements”, Exp Fluids 49, 1375-1391, (2010).

Crowe C. T. (Editor), “Multiphase Flow Handbook”, CRC Press, (2006).

Glovier A. R., Skippon S. M. and Boyle R. D., “Interferometric laser imaging for droplet sizing: A method for droplet-size measurement in sparse spray systems”, Appl Opt 34, 8409–8421, (1995).

Gui L. C., Lindken R. and Merzkirch W., “Phase-separated PIV measurements of the flow around systems of bubbles rising in water”, ASME-FEDSM97-3103, (1997).

Hassan, Y. A., Blanchat, T. K., Seeley, C. H. and Canaan, R. E., “Simultaneous velocity measurements of both components of a two-phase flow using particle image velocimetry”, Int. J. Multiphase Flow 18, 371-395, (1992).

Hassan, Y. A. and Canaan, R. E., “Full-field bubbly flow velocity measurements using a multiframe particle tracking technique”, Exp Fluids 12, 49-60, (1991).

Hassan, Y. A., Philip, O. G. and Schmidl, W. D., “Bubble collapse velocity measurements using a particle image velocimetry technique with fluorescent tracers”, ASME FED 172, 85-92, (1993).

Hassan Y. A., Schmidl W. and Ortiz-Villafuerte J., “Investigation of three-dimensional two phase flow structure in a bubbly pipe flow”, Meas Sci Tech 9, 309-326, (1998).

Honkanen M., “Turbulent Multiphase Flow measurement with Digital Particle Image velocimetry”, M.S. Thesis, Tampere University of technology, (2002).

Koenig G., Anders K. and Frohn A., “A new light-scattering technique to measure the diameter of periodically generated moving droplets”, J Aerosol Sci 17, 157–167, (1986).

Lacagnina G., Grizzi S., Falchi M., Felice Di F. and Romano G. P., "Simultaneous size and velocity measurements of cavitating microbubbles using interferometric laser imaging", Exp Fluids 50, 1153-1167, (2011).

Lindken R. and Merzkirch W., "Velocity measurements of liquid and gaseous phase for a system of bubbles rising in water", Exp Fluids [suppl.], 194-201, (2000).

Lindken R. and Merzkirch W., "A novel PIV technique for measurements in multiphase flows and its application to two phase bubbly flows", Exp Fluids 33, 814–825, (2002).

Maeda M., Kawaguchi T. and Hishida K., "Novel interferometric measurement of size and velocity distributions of spherical particles in fluid flows", Meas Sci Tech 12, L13–L18, (2000).

Naito M., Inoue M., Ichiyanagi M., Sato Y. and Hishida K., "Development of two-color digital holographic PTV for dispersed two-phase flow". The 6th International Symposium on Measurement Techniques for Multiphase Flows. Journal of Physics 147 (2009).

Ortiz-Villafuerte J., Schimdl W. D. and Hassan Y. A., "Three dimensional PTV study of the surrounding flow and wake of a bubble rising in a stagnant liquid", Exp Fluids, S202-S210, (2000).

Palero V., Lobera J. and Arroyo M. P., "Digital image plane (DIPH) for two-phase flow diagnostics in multiple planes", Exp Fluids 39, 397-406, (2005).

Reese J., Chen R. C. and Fan L. S., "Three dimensional particle image velocimetry for use in three phase fluidization system", Exp Fluids 19, 367-378, (1995).

Schnars U. and Jueptner W., "Digital Holography", Springer, Berlin, (2005).

Sheng J., Malkiel E. and Katz J., "Digital holographic microscope for measuring three dimensional particle distributions and motions", Appl Optics, 45, 3893-3901, (2006).

Sridhar G. and Katz J., "Lift and drag forces on microscopic bubbles entrained by a vortex", Phys Fluids 7, 389–399, (1995).

Sveen J. and Cowen E., "An introduction to MatPIV v 1.6.1", eprint series, Dept of Math. University of Oslo, ISSN 0809-4403, (2004).

Tian L., Loomis N., Dominguez-Caballero J. and Barbastathis G., "Quantitative measurement of size and three-dimensional position of fast-moving bubbles in air-water mixture flows using digital holography", Appl Optics 49, 1549-1554, (2010).

Yamamoto F., Murai Y. and Ishikawa, “Particle Tracking Velocimetry for Dispersions in Multiphase Flows”, 4th International Symposium on Particle Image Velocimetry, Göttingen, Germany, Sep. 17-19, Paper 1064, (2001).

APPENDICES

A.1. Matlab program for hologram reconstruction

```
clc
disp('Step 1. Read the image file into matrix');
h=imread('seeded_bubble_0004A','TIF');
[Ny Nx Nz]=size(h);
if Nz>1
h=rgb2gray(h);
end
h0=double(h);
[Ny Nx]=size(h0); %Ny= number of rows Nx= number of column
if Nx>Ny %remove the extra column to make image square
S=Nx-Ny;
h0(:,1:S/2)=[];
h0(:,Ny+1:Nx-S/2)=[];
elseif Nx<Ny %remove the extra rows to make image square
S=Ny-Nx;
h0(1:S/2,:)=[];
h0(Nx+1:Ny-S/2,:)=[];
end
disp('dimensions of the images');
[Ny Nx]=size(h0);
```

```
lambda=.532; %the wavelength of laser in micron

dxh=7.8;

dyh=7.8;

M=2; %Enter desired magnification (this will change location of focused image)%

first=50; %first reconstruction distance

last=400; %last reconstruction distance

step=10; %step size for reconstruction images

disp('Step 2. Numerical reconstruction of the images');51

A=ones(Ny,Nx);

if(Ny>Nx)

coef0=diag(1:Ny)*ones(Ny);

else

coef0=diag(1:Nx)*ones(Nx);

end

coef1=coef0(1:Ny,1:Nx);

coef2=coef0(1:Nx,1:Ny)';

for D = first: step: last; %Input the range of reconstruction distances in mm must be
between 200mm and 800mm with minimum spacing of 1mm

disp('Reconstruction in progress.....');

d=D*1000; %converts to microns%

dr=240; %distance from source point to CCD in recording phase%

dr=dr*1000; %converts to microns%

xrprime=Nx/2; %location of source point in reconstruction phase (usually centered)%

yrprime=Ny/2; %location of source point in reconstruction phase (usually centered)%

dprime=d*M; %reconstruction distance%
```

```
drprime=(1/dprime-1/d+1/dr)^(-1); %location of source point in reconstruction phase%

coff1=((dprime^2)*A+((coef1-(A*Nx/2)).^2)*(dxh^2)+((coef2-
(A*Ny/2)).^2)*(dyh^2)).^0.5;

g =(1i/lambda)*(exp((-1i*2*pi/lambda)*coff1))./coff1;

Er =exp(-1i*2*pi/lambda*(A*drprime^2+(coef1-A*xrprime).^2+(coef2-
A*yrprime).^2).^0.5); %Equation for spherical reference beam%

H0=fftshift(fft2(h0.*Er)); %eq. 3.32

G=fftshift(fft2(g)); %eq. 3.32

h_Amp=fftshift(ifft2(H0.*G)); %eq. 3.32

I=(h_Amp.*conj(h_Amp)); %Multiplies U0 with the complex conjugate of U0% to get
the image intensity

B=max(max(I));

I=I./B;

Imin=min(min(I));

Imax=max(max(I));

I=imadjust(I,[Imin; Imax],[]);

I=(I.^(1/6));

imwrite(I,[num2str(D) '_mm.TIF']);

End
```

B.1. Results for other Images with interrogation window size of 256 pixels

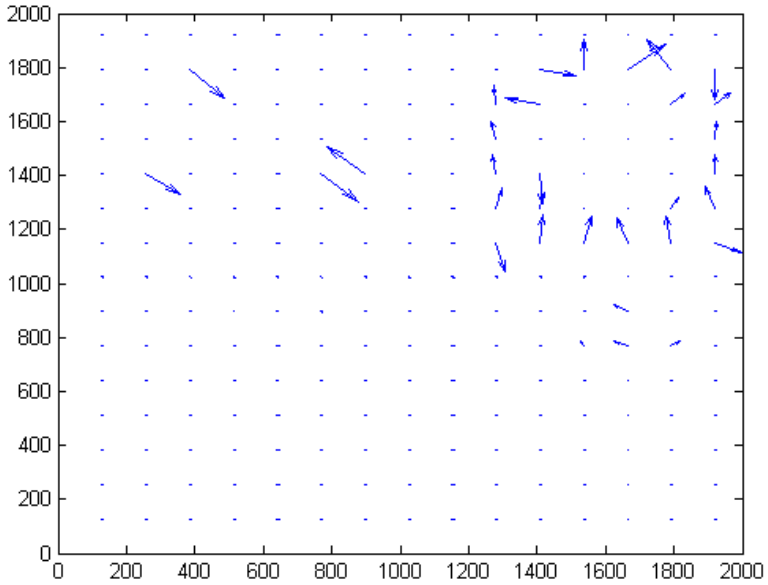

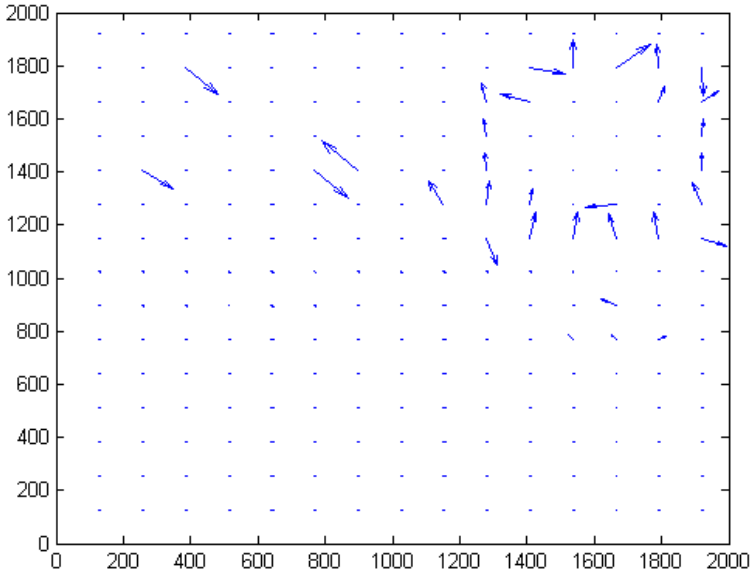

B.2. Results for other Images with improper thresholding

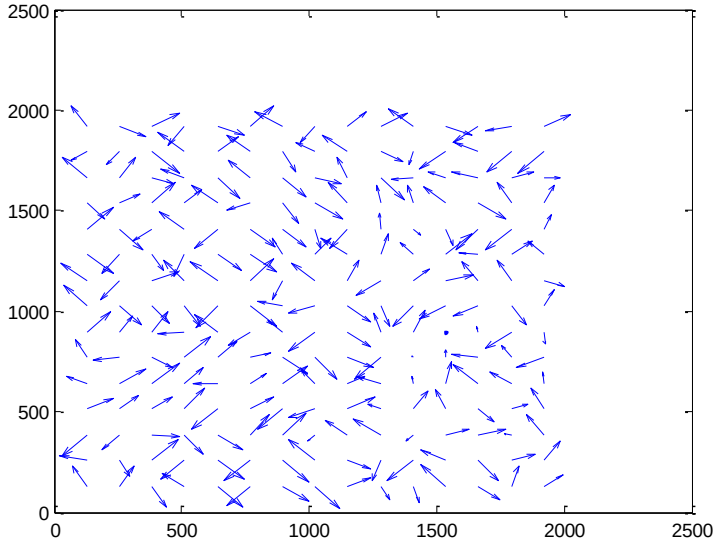

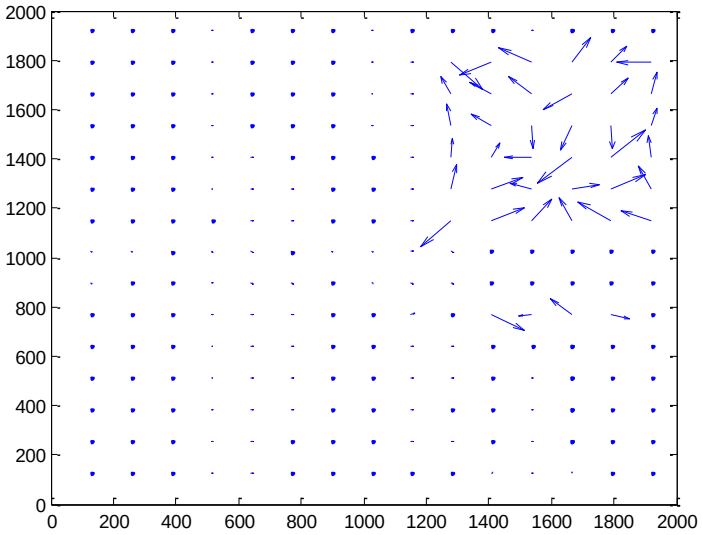

B.3. Results for Images with interrogation window size of 512 pixels

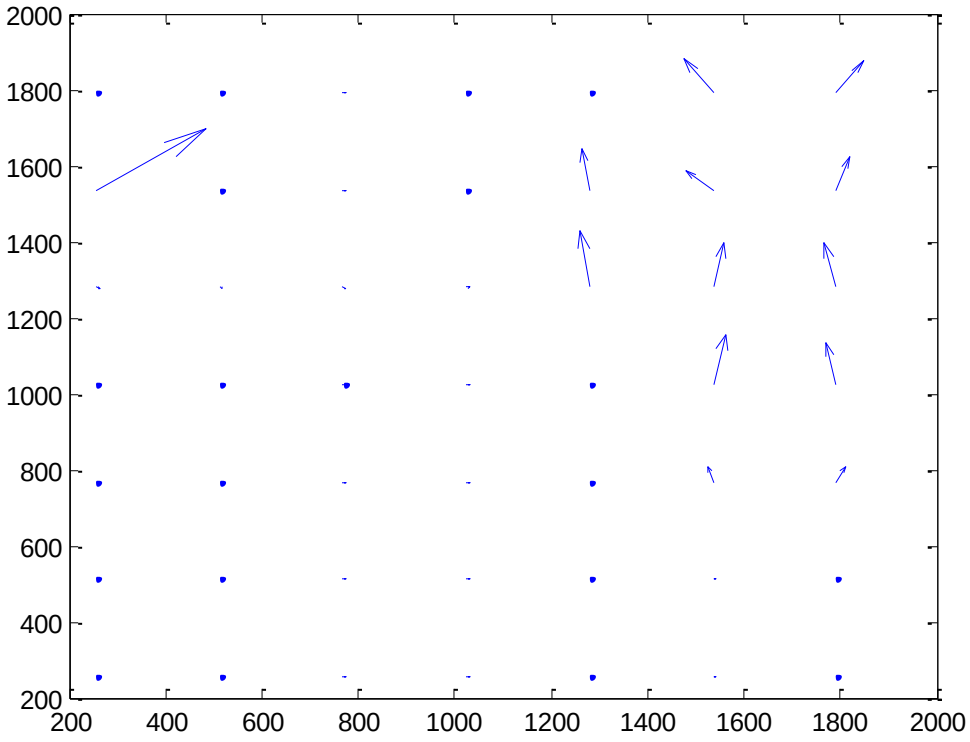

VITA

Atanu Banerjee

Candidate for the Degree of

Master of Science

Thesis: APPLICATION OF HOLOGRAPHIC PARTICLE IMAGE VELOCIMETRY IN BUBBLY FLOW

Major Field: Mechanical and Aerospace Engineering

Biographical: Atanu Banerjee is the son of A. K. Banerjee and Seema Banerjee and a resident of Durgapur, West Bengal, India.

Education: Received B.Tech (Mechanical Engineering) from West Bengal University of Technology, West Bengal in 2010 pursuing the requirements for Master of Science in Mechanical and Aerospace Engineering at Oklahoma State University, Stillwater, Oklahoma.

Experience: Employed by Oklahoma State University as Teaching Assistant for Thermodynamics II, Alternative Energy Systems and Compressible Flows from Fall 2010 to Spring 2012.